

Ultra-low Frequency Foreshock Waves and Ion Dynamics at Mars

R. Jarvinen^{1,2}, E. Kallio¹ and T. I. Pulkkinen^{3,1}

¹Department of Electronics and Nanoengineering, School of Electrical Engineering, Aalto University, Espoo, Finland

²Finnish Meteorological Institute, Helsinki, Finland

³Department of Climate and Space Sciences and Engineering, University of Michigan, Ann Arbor, Michigan, USA

Key Points:

- Two distinct foreshock ULF wave regions form in a global Mars-solar wind interaction hybrid simulation.
- The ULF waves modulate ion precipitation and escape at Mars.
- Ionospheric oxygen ion escape is enhanced by 60-70% under radial IMF.

Corresponding author: R. Jarvinen, riku.jarvinen@aalto.fi

This article has been accepted for publication and undergone full peer review but has not been through the copyediting, typesetting, pagination and proofreading process, which may lead to differences between this version and the [Version of Record](#). Please cite this article as [doi: 10.1029/2021JA030078](https://doi.org/10.1029/2021JA030078).

This article is protected by copyright. All rights reserved.

Abstract

We study the solar wind interaction with Mars in a global three-dimensional hybrid model. A well-developed, vast ion foreshock forms under a strongly flow-aligned interplanetary magnetic field (IMF) configuration but otherwise nominal solar wind and solar minimum photon flux conditions. Large-scale ultra-low frequency (ULF) waves are excited in the foreshock by backstreaming ions. The foreshock ULF waves constitute two distinct regions in the analyzed solar wind and IMF situation: the near region where the wave period is 71-83 s and the far region where the wave period is 25-28 s. The near foreshock region waves transmit downstream through the bow shock and affect dynamics of the solar wind and planetary ion populations. Especially, ion precipitation rate into the exobase and planetary ion escape rates fluctuate at the ULF wave period corresponding to the near foreshock region. The peak-to-peak amplitude of the modulation is few percent or less. Interestingly, ionospheric oxygen ion escape fluxes show more than two orders of magnitude local modulations in the heavy plume at the same period. Finally, the escape rates of the ionospheric oxygen ion populations are enhanced by 60-70% under flow-aligned IMF compared to nominal upstream conditions.

1 Introduction

Mars being the solar system's smallest planet with an atmosphere has a unique interaction with the solar wind. An induced planetary magnetosphere is formed when the solar wind interacts with an ionosphere of a globally unmagnetized planet like Mars and Venus (*Lundin, Lammer, and Ribas, 2007*). The highly conductive dayside ionosphere causes the magnetized solar wind plasma flow to deviate around the planet. In this process, a magnetic barrier and an induced magnetosphere are formed. A bow shock is formed as the outermost boundary of a planetary plasma environment because the solar wind flow is typically supermagnetosonic. That is, the solar wind slows down and heats up when passing from the upstream to the downstream at the bow shock. The downstream region of turbulent, shocked plasma is called the magnetosheath. The magnetosheath is separated from the planetary plasma dominated region and the planetary wake by the induced magnetospheric boundary or the ionopause.

The compact size of Mars and its plasma environment mean that the finite Larmor radius effects play an essential role in dynamics of escaping heavy planetary ions (*Kallio and Jarvinen, 2012*). Since an induced magnetosphere forms by the piling up of the interplanetary magnetic field (IMF) lines against an ionosphere, the solar wind flows close to the upper atmosphere and through the exosphere allowing direct acceleration of planetary ions by the electric fields associated with an induced magnetosphere and the solar wind (*Brain, Bagenal, Ma, Nilsson, and Stenberg Wieser, 2016*). A portion of the accelerated planetary ions reach escape velocities from the Martian gravity well via several different escape channels or acceleration mechanisms and are lost to space (*Dubinin, Fraenz, Fedorov, Lundin, Edberg, Duru, and Vaisberg, 2011*). The planetary ion acceleration is driven by the solar wind interaction, but the total escape rate is affected also by the solar photon flux conditions (*Nilsson, Carlsson, Brain, Yamauchi, Holmström, Barabash, Lundin, and Futaana, 2010; Ramstad, Barabash, Futaana, Nilsson, Wang, and Holmström, 2015*).

Several of the escape channels are associated with steady-state acceleration mechanisms like the planetary ion pickup by the solar wind and the formation of the heavy ion plume (*Dong, Fang, Brain, McFadden, Halekas, Connerney, Eparvier, Andersson, Mitchell, and Jakosky, 2017; Futaana, Stenberg Wieser, Barabash, and Luhmann, 2017*). In addition, also dynamical processes can affect planetary ion acceleration in induced magnetospheres (*Dubinin, Fraenz, Pätzold, Tellmann, Woch, McFadden, and Zelenyi, 2021; Jarvinen, Alho, Kallio, and Pulkkinen, 2020a; Luhmann, Russell, Phillips, and Barnes, 1987; Lundin, Barabash, Dubinin, Winningham, and Yamauchi, 2011; Omidi, Collinson,*

65 and Sibeck, 2020). Especially, a foreshock is formed in the upstream region by backstream-
 66 ing charged particle populations scattered near the bow shock (Brain, Bagenal, Acuña,
 67 Connerney, Crider, Mazelle, Mitchell, and Ness, 2002; Eastwood, Lucek, Mazelle, Meziane,
 68 Narita, Pickett, and Treumann, 2005; Mazelle, Winterhalter, Sauer, Trotignon, Acuña,
 69 Baumgärtel, Bertucci, Brain, Brecht, Delva, Dubinin, Øieroset, and Slavin, 2004). The
 70 ion foreshock forms in the region with a magnetic connection to the quasi-parallel bow
 71 shock where the angle between an outwards shock surface normal and the magnetic field
 72 is small enough allowing ion scattering ($< 45^\circ$). The backstreaming particles are a source
 73 of free energy for plasma instability excitation, and, thus, the foreshock is rich in plasma
 74 structures and waves including prominent, large amplitude, magnetosonic ultra-low fre-
 75 quency (ULF) waves, which are observed at all solar system’s terrestrial planets (Delva
 76 and Dubinin, 1998; Dubinin and Fraenz, 2016; Hoppe and Russell, 1982; Le, Chi, Blanco-
 77 Cano, Boardsen, Slavin, Anderson, and Korth, 2013). This way the foreshock ”prepro-
 78 cesses” the solar wind before it encounters the quasi-parallel bow shock.

79 The orientation of the upstream IMF vector determines the location and extent of
 80 the foreshock. The IMF has two main polarities associated with the Parker spiral and
 81 different sides of the heliospheric current sheet: the toward (the Sun) sector ($B_x > 0, B_y <$
 82 0) and the away (from the Sun) sector ($B_x < 0, B_y > 0$) (Parker, 1958). The Parker
 83 spiral angle, the angle between the IMF vector and the assumed radial solar wind ve-
 84 locity vector, is typically about 57° (away sector) or $180^\circ - 57^\circ = 123^\circ$ (toward sec-
 85 tor) at Mars (Slavin and Holzer, 1981). However, the IMF and the solar wind vary con-
 86 stantly and other conditions like closely flow-aligned IMF occur regularly (Liu, Rong,
 87 Gao, He, Klinger, Dunlop, Yan, Fan, and Wei, 2021; Luhmann, Zhang, Petrinec, Rus-
 88 sell, Gazis, and Barnes, 1993). Strongly flow-aligned (radial) IMF conditions are inter-
 89 esting in the context of the current study since they result in the dayside foreshock and
 90 quasi-parallel bow shock ahead of the subsolar region (Fowler, Halekas, Schwartz, Goodrich,
 91 Gruesbeck, and Benna, 2019; Halekas, Ruhunusiri, Harada, Collinson, Mitchell, Mazelle,
 92 McFadden, Connerney, Espley, Eparvier, Luhmann, and Jakosky, 2017). Conversely, strongly
 93 perpendicular IMF vector means that the bow shock is mostly quasi-perpendicular in
 94 the dayside of the planet and no proper subsolar foreshock forms under the solar min-
 95 imum photon flux conditions. At solar maximum, upstream ULF waves are expected to
 96 be excited even under nominal IMF conditions (Parker spiral angle 57°) due an extended
 97 hydrogen exosphere and an enhanced photoionization compared to solar minimum (Bertucci,
 98 Romanelli, Chaufray, Gomez, Mazelle, Delva, Modolo, González-Galindo, and Brain,
 99 2013; Chaffin, Chaufray, Stewart, Montmessin, Schneider, and Bertaux, 2014; Delva and
 100 Dubinin, 1998; Romanelli, Mazelle, Chaufray, Meziane, Shan, Ruhunusiri, Connerney,
 101 Espley, Eparvier, Thiemann, Halekas, Mitchell, McFadden, Brain, and Jakosky, 2016;
 102 Yamauchi, Hara, Lundin, Dubinin, Fedorov, Sauvaud, Frahm, Ramstad, Futaana, Holm-
 103 strom, and Barabash, 2015).

104 In addition to affecting the bow shock dynamics, the ULF foreshock waves trans-
 105 mit through the bow shock and travel in the magnetosheath and near the ionosphere and
 106 the exobase at Mars (Collinson, Wilson, Omid, Sibeck, Espley, Fowler, Mitchell, Gre-
 107 bowsky, Mazelle, Ruhunusiri, Halekas, Frahm, Zhang, Futaana, and Jakosky, 2018). In
 108 the process, the ULF waves heat the dayside ionosphere and likely cause substantial plan-
 109 etary ion outflow (Fowler, Andersson, Ergun, Harada, Hara, Collinson, Peterson, Es-
 110 pley, Halekas, Mcfadden, Mitchell, Mazelle, Benna, and Jakosky, 2018). The ULF waves
 111 are also likely responsible for other dynamical ion processes like the dispersed ion ener-
 112 gization events observed at Mars (Collinson *et al.*, 2018; Halekas, McFadden, Conner-
 113 ney, Espley, Brain, Mitchell, Larson, Harada, Hara, Ruhunusiri, and Jakosky, 2015).
 114 Further, charge exchange upstream of the bow shock is thought to be modulated by fore-
 115 shock processes and these fluctuations are observed at low altitudes as penetrating pro-
 116 tons resulting from a secondary charge exchange (Fowler *et al.*, 2019). All in all, the fore-
 117 shock is a highly dynamical region and could play a major role in the acceleration of es-
 118 caping planetary ions.

119 Here we present results on the foreshock ULF waves and their modulation of the
 120 plasma environment and ion escape and precipitation at Mars in a global hybrid sim-
 121 ulation model. In the next section we describe the most important features of the model
 122 to this study as well as the simulation run setup. Then we present our results on the over-
 123 all structure of the Mars plasma environment and analyze the foreshock ULF waves and
 124 their effects near Mars in detail. Then we discuss the results and compare them to ear-
 125 lier theoretical and observations works. At the end we summarize our findings.

126 2 Model

127 We use our highly parallelized global hybrid model to analyze the Mars-solar wind
 128 interaction (*Jarvinen, Brain, Modolo, Fedorov, and Holmström, 2018; Jarvinen et al.,*
 129 *2020a; Jarvinen, Alho, Kallio, and Pulkkinen, 2020b*). In the model, ions are treated as
 130 macroscopic particle clouds (macroparticles) moving under the Lorentz force using a leap-
 131 frog algorithm. Each macroparticle represents a number of real physical particles described
 132 by the statistical weight of the macroparticle. Electrons form a charge-neutralizing and
 133 massless fluid. The magnetic field is advanced by Faraday’s law and the total electric
 134 current density comes from Amperè’s law. This way the ion dynamics (the ion charge
 135 density and the ion electric current density) are self-consistently coupled with the evo-
 136 lution of the magnetic field. Magnetized solar wind is injected in the simulation from the
 137 front ($+x$) wall and all walls allow free outflow of the plasma. The planetary obstacle
 138 (the inner boundary) to the solar wind flow is modeled as a superconducting sphere near
 139 the exobase, which the magnetic field cannot penetrate. Macroparticles entering the in-
 140 ner boundary are assumed precipitated and are removed from the simulation. The model
 141 equations and numerical schemes are the same as in our earlier studies with the excep-
 142 tion of the electron pressure description. In this study, we use the scalar electron pres-
 143 sure term in Ohm’s law, which assumes the ideal gas law in the adiabatic approxima-
 144 tion with the polytropic index $\gamma = 2$ corresponding to two degrees of freedom perpen-
 145 dicular to the magnetic field. Further details of the algorithm can be found in *Kallio and*
 146 *Janhunen (2002,0)*.

147 Four major Mars planetary ion populations are used in the simulation runs ana-
 148 lyzed here. The populations are similar than in our earlier Mars works. The ionospheric
 149 atomic (O_{iono}^+) and molecular ($O_{2,\text{iono}}^+$) oxygen ions are emitted in the simulation at
 150 the model’s inner boundary. The ionospheric emission has a $\cos(\text{solar-zenith angle})$ de-
 151 pendence on the dayside and a constant nightside emission of 10% of the noon emission.
 152 The ionospheric ions are emitted with a Maxwellian velocity distribution and the tem-
 153 perature of 2×10^4 K (*Jarvinen, Kallio, Janhunen, Barabash, Zhang, Pohjola, and Sil-*
 154 *lanpää, 2009*). The emission rates of the ionospheric populations are selected so that they
 155 match *in situ* observations (*Jarvinen et al., 2018*). Moreover, photoions are produced
 156 from exospheric neutral coronae. This includes hot exospheric oxygen (O_{exo}^+) and hy-
 157 drogen (H_{exo}^+) populations. The solar minimum photon flux ionization conditions are
 158 applied. Specifically, the neutral profiles are from ”Run B (solar min, with exosphere)”
 159 of the ”Intercomparison of Global Models and Measurements of the Martian Plasma En-
 160 vironment” International Space Science Institute (ISSI) team’s second meeting (*Brain,*
 161 *Barabash, Boeswetter, Bougher, Brecht, Chanteur, Hurley, Dubinin, Fang, Fraenz, Halekas,*
 162 *Harnett, Holmstrom, Kallio, Lammer, Ledvina, Liemohn, Liu, Luhmann, Ma, Modolo,*
 163 *Nagy, Motschmann, Nilsson, Shinagawa, Simon, and Terada, 2010a; Egan, Ma, Dong,*
 164 *Modolo, Jarvinen, Bougher, Halekas, Brain, Mcfadden, Connerney, Mitchell, and Jakosky,*
 165 *2018; Jarvinen et al., 2018; Kallio, Liu, Jarvinen, Pohjola, and Janhunen, 2010; Mod-*
 166 *olo, Hess, Mancini, Leblanc, Chaufray, Brain, Leclercq, Esteban-Hernández, Chanteur,*
 167 *Weill, González-Galindo, Forget, Yagi, and Mazelle, 2016*). The profiles are spherically
 168 symmetric and they are based on results by the Mars Thermosphere General Circula-
 169 tion Model (MTGCM) (parameters $L_s = 270$ and $F_{10.7} = 34$) (*Bougher, Blelly, Combi,*
 170 *Fox, Mueller-Wodarg, Ridley, and Roble, 2008*) and the Direct Simulation Monte Carlo

171 (DSMC) dissociative recombination model for the Martian hot oxygen densities (*Vaille,*
172 *Combi, Tenishev, Bougher, and Nagy, 2010*).

173 The solar wind ions consist of proton (H_{SW}^+) and alpha (He_{SW}^{++}) populations; these
174 refer to full populations including the incident solar wind core and the suprathermal/backstreaming
175 foreshock beam, unless otherwise stated. The injection rates of all solar wind and plan-
176 etary ion populations in the simulation domain are constant in time. The average num-
177 bers of macroparticles per grid cell are: Run 1: 175 (H_{SW}^+), 9 (He_{SW}^{++}), 19 (O_{iono}^+), 19 ($O_{2,\text{iono}}^+$),
178 25 (H_{exo}^+) and 29 (O_{exo}^+); Run 2: 177 (H_{SW}^+), 9 (He_{SW}^{++}), 15 (O_{iono}^+), 16 ($O_{2,\text{iono}}^+$), 7 (H_{exo}^+)
179 and 9 (O_{exo}^+) in Run 2. However, note that the density, and, thus, the number of macropar-
180 ticles per cell is highly variable for each population in the simulation domain.

181 Two three-dimensional simulation runs were performed for this study. Run 1 uses
182 a highly flow-aligned (radial) IMF with the 6° spiral angle to allow the formation of an
183 extensive, dayside ion foreshock in the simulation domain. Run 2 uses the nominal Parker
184 Mars IMF with the spiral angle of 57° as a control case. Other than the IMF spiral an-
185 gles the runs have an identical setup corresponding to the nominal Mars upstream con-
186 ditions (*Slavin and Holzer, 1981*). Note that we choose to change only one parameter,
187 the IMF flow-aligned component, between the two runs. This allows us to distinguish
188 its effect in the Mars-solar wind interaction in a reliable way. In practice, also other up-
189 stream conditions can co-vary with the spiral angle, and the average conditions can vary
190 from solar minimum to solar maximum. To further simplify the situation, the Mars crustal
191 magnetic anomalies and charge exchange and electron impact ionization of the exosphere
192 are not included in the analyzed simulation runs.

193 Temporal scales include ion gyro periods of 20 s (H^+), 39 s (He^{++}), 316 s (O^+) and
194 631 s (O_2^+) in the undisturbed solar wind. Thermal gyro radii of the solar wind species
195 are 123 km (H^+) and 229 km (He^{++}) and gyro radii of the heavy pickup ions are 2258
196 km (O^+) and 4517 km (O_2^+) in the undisturbed upstream solar wind in the radial IMF
197 run.

198 The simulations were run for 1000 s and the initialization and the formation of the
199 foreshock took about 300 s. The analysis period was from $t = 500..800$ s, which includes
200 about 4 periods of the near region ULF waves and 11 periods of the far region ULF waves.

201 See Table 1 for details of the numerical setup and the physical parameters of the
202 simulation runs.

203 2.1 Coordinate system

204 The model uses a planet-centered coordinate system. The x -axis is antiparallel to
205 the incident, undisturbed solar wind flow, the y -axis is aligned along the perpendicular
206 IMF component to the undisturbed solar wind flow, and the z -axis completes the right-
207 handed coordinate system. Consequently, the z -axis is along the convection electric field
208 in the undisturbed solar wind. The hemisphere where the upstream solar wind convec-
209 tion electric field points away from the planet ($z > 0$) is termed the $+E_{\text{SW}}$ hemisphere
210 and the $y < 0$ hemisphere is termed the foreshock hemisphere. The radius of Mars (R_{M}
211 = 3390 km) is used as the unit of length in the figures and the text.

212 Virtual spacecraft time series were recorded in three points (P1-P3) and ion veloc-
213 ity distributions in two points (P1 and P4):

$$\begin{aligned} \text{P1} &= (x = 2.63, y = -0.57, z = -0.03)R_{\text{M}} && \text{(dayside foreshock / near region)} \\ \text{P2} &= (x = 1.23, y = -0.57, z = -0.03)R_{\text{M}} && \text{(subsolar magnetosheath)} \\ \text{P3} &= (x = -0.23, y = -0.03, z = 1.98)R_{\text{M}} && \text{(heavy ion plume)} \\ \text{P4} &= (x = -0.23, y = -4.43, z = -0.03)R_{\text{M}} && \text{(far region)}. \end{aligned}$$

214

See Figs. 3b-c for the locations of the points.

215

3 Model results

216

3.1 Large-scale structure

217

218

219

220

221

222

223

Fig. 1 shows an overview of the solar wind proton kinetic, scalar temperature near Mars in both model runs. In the nominal run, the induced magnetosphere is well-formed and the IMF is piled up against the ionospheric obstacle forming the magnetic barrier. The induced magnetosphere is seen as increased temperature downstream of the bow shock compared to the undisturbed upstream region. In the radial IMF run, the boundaries of the induced magnetosphere are less well-defined due to the lack of a strong magnetic barrier.

224

225

226

227

228

229

230

231

The ion foreshock is seen in the $y < 0$ hemisphere as elevated upstream temperatures caused by the solar wind protons that are scattered upstream at the quasi-parallel bow shocks. In the nominal run, the quasi-parallel bow shock is at larger than 90° solar-zenith angles near the back ($-x$) wall of the simulation domain and, thus, no proper foreshock forms close to the planet. In the radial IMF run, the quasi-parallel bow shock covers a large part of the $y < 0$ hemisphere on the $z = 0$ plane and the foreshock forms already in the near subsolar region. Top panels of Movie S01 (supplementary material) show the dynamics of the temperature and the formation of the foreshock.

232

233

234

235

236

237

238

Fig. 2 compares the magnetic field B_z component in both runs. B_z is the perpendicular component to the undisturbed solar wind velocity and IMF vectors. Consequently, any non-zero B_z values are associated with the Mars-solar wind interaction. Large-scale ULF waves are evident in the foreshock in the radial IMF run ($y < 0$ hemisphere). A minor B_z upstream disturbance is seen in the nominal run close to the back wall but no clear ULF waves occur. The propagation of the waves can be seen in the bottom panels of Movie S01 (supplementary material).

239

240

241

242

243

244

245

246

247

248

249

250

Fig. 3 gives an overview of the planetary O^+ density in the model. The exospheric photoions are seen as a spherical cloud reaching high-altitudes around the planet. Ionospheric ion emission is seen at lowest altitudes where the density is the highest. In the nominal run, the O^+ density is almost symmetric between the $y > 0$ and $y < 0$ hemispheres due to the small flow-aligned IMF component (B_x). That is, small B_x results in a small angle between the upstream solar wind velocity and the $E \times B$ drift velocity vectors. On the other hand, the radial IMF run has strong hemispheric asymmetries on the xy plane associated with highly perpendicular $E \times B$ drift to the solar wind velocity. The orientations of the upstream $E \times B$ velocity vectors are shown in Figs. 3b,e. Both runs have strong hemispheric asymmetry in the direction of the convection electric field caused by the solar wind ion pickup. Movie S02 (supplementary material) shows the dynamics of the O^+ ion density.

251

252

This concludes the comparative analysis of the two simulation runs. From here on we concentrate on the radial IMF run (Run 1) where a proper foreshock forms near Mars.

253

3.2 Foreshock and ULF waves in the radial IMF run

254

255

256

257

258

259

260

Fig. 4 displays spatial distribution of the B_z times series in the foreshock. Each insert shows $B_z(t)$ over a 500-s interval recorded in the simulation. The vertical axis has the height of 1 nT in all inserts and the axis is centered at the mean value. The full detailed version of the inserts is shown in Fig. 5. The figures show that a range of different wave periods and amplitudes populate the foreshock. Largest absolute wave amplitudes occur around the lower left corner of Figs. 4-5, where also the strongest ULF waves are seen in Fig. 2 and Movie S01 (supplementary material).

261 The $B_z(t)$ time series were Fourier transformed and they are shown in Fig. 6. Then
 262 the period of the main ULF wave frequency was determined from the Fourier transfor-
 263 mation (red circles in Fig. 6), and the resulting periods are shown in Fig. 7a. Two dis-
 264 tinct wave regions are clearly identified. The lowest altitudes and the subsolar region show
 265 mostly longer wave periods between 71-83 s (the near region or the 83-s waves). Shorter
 266 periods of 25-28 s are found farther away from the planet where the wave amplitudes are
 267 the strongest (the far region or the 28-s waves). In addition, it can be seen in Fig. 7b
 268 that the ULF waves have largely positive correlation between the plasma density and
 269 the magnetic field throughout the foreshock.

270 The foreshock waves are analyzed in more detail in Figs. 8 and 9, where minimum
 271 variance analysis (MVA) and hodograms of the magnetic field are shown in the two re-
 272 gions. The locations where the hodograms are determined are denoted with dashed line
 273 in Fig. 4. As can be seen in Fig. 8, the waves in the near region are strongly elliptically
 274 polarized and propagate at an angle $\cos^{-1}(\hat{b} \cdot \hat{k}) = 89^\circ$. The propagation is nearly per-
 275 pendicular to the magnetic field in most of the near region. There is no fixed handed-
 276 ness of the wave polarization in the near region, but both left-handed to right-handed
 277 rotations are found.

278 Fig. 9 shows the hodogram in the far region. It can be seen that the polarization
 279 here is closer to circular compared to the near region. The propagation angle is $\cos^{-1}(\hat{b} \cdot \hat{k}) = 48^\circ$
 280 in the analyzed point but it varies between $20\text{-}50^\circ$ in the far region. The waves
 281 rotate in a left-handed sense with respect to the magnetic field in the simulation frame
 282 consistently throughout the far region.

283 3.3 Ion velocity distributions in the foreshock

284 Fig. 10 shows velocity distributions of the solar wind protons in the near and far
 285 foreshock regions at P1 and P4 (Fig. 3b-c). The incident solar wind core is visible as a
 286 spherically symmetric population near the undisturbed upstream bulk velocity of $[-430, 0, 0]$
 287 km/s. The wide suprathermal (beam) population scattered at the bow shock is located
 288 away from the incident core antiparallel to the magnetic field. The suprathermal pop-
 289 ulation is much wider and has a temperature of about one to two orders of magnitude
 290 higher than the core. Table 2 lists bulk properties of the core and suprathermal ion pop-
 291 ulations in Fig. 10.

292 A major part of the near region suprathermal population is backstreaming ($v_x >$
 293 0) and the population has a bulk velocity of $[262, 0, -77]$ km/s in the simulation frame.
 294 In the far region, the major part of the suprathermal population is found between $v_x =$
 295 $-250 \dots 0$ km/s and the population has a bulk velocity of $[-53, -120, -25]$ km/s with only
 296 a small fraction backstreaming in the simulation frame. However, if the velocity distri-
 297 butions are transformed in the rest frame of the core, it can be seen that both the near
 298 and far region suprathermal populations are backstreaming towards the incident flow.
 299 The average density of the suprathermal beam varies from below 1% up to about 10%
 300 of the core in the foreshock.

301 3.4 Virtual spacecraft time series

302 In order to analyze the foreshock plasma dynamics and the propagation of ULF
 303 waves near Mars in detail, time series of different quantities were determined in three
 304 points P1-P3 (Fig. 3b-c).

305 Fig. 11 shows the dayside foreshock point P1. The positively correlated fluctua-
 306 tions of the solar wind ion densities and the magnetic field at the ULF wave period of
 307 83 s are evident. The exospheric H_{exo}^+ density shows also weak ULF fluctuations while
 308 the exospheric O_{exo}^+ density is dominated by statistical macroparticle noise.

309 Closer to the planet in the subsolar magnetosheath (P2) the ULF fluctuations be-
 310 come more pronounced than in the upstream foreshock as can be seen in Fig. 12. Note
 311 that P1 and P2 are at the same line parallel to the x -axis. Overall, the fluctuations have
 312 larger amplitude at P2 than at P1. Also the exospheric O_{exo}^+ density shows strong fluctu-
 313 ations at the ULF period at P2. However, the maxima of oxygen densities are delayed
 314 compared to the maxima of the solar wind and exospheric H_{exo}^+ densities and the mag-
 315 netic field strength.

316 Fig. 13 displays the point P3 in the heavy ion plume ($+E_{\text{SW}}$ hemisphere). Here
 317 the magnetic field does show as smooth, near sinusoidal ULF fluctuations as at P1 and
 318 P2, but the waveforms are more steepened or sawtooth type. The solar wind and exo-
 319 spheric ion densities do not fluctuate clearly in concert with the magnetic field. How-
 320 ever, the plume has high ionospheric O_{iono}^+ and $O_{2,\text{iono}}^+$ density and both of them show
 321 sharp increases in concert with the magnetic field wavefronts at near the ULF foreshock
 322 period. The maxima of O^+ densities occur before O_2^+ maxima, which can be understood
 323 as the two populations undergoing the same accelerating force associated with the ULF
 324 waves after being emitted from the inner boundary and the heavier population (O_2^+) lack-
 325 ing slightly behind.

326 Fig. 14 analyzes the plume O_2^+ population in detail. It can be seen that the den-
 327 sity spikes are associated with periodic time-energy spectrogram structures, where the
 328 velocity increases in concert with the density spikes. The velocity increase is directed along
 329 $v_y < 0$ and $v_z > 0$ direction, that is, towards the $+E_{\text{SW}}$ hemisphere and the foreshock
 330 hemisphere.

331 3.5 Ion escape and precipitation

332 Fig. 15 shows the time series of planetary ion escape rates from the simulation do-
 333 main and the solar wind ion precipitation rates in the inner boundary in the radial IMF
 334 run. Table 3 lists time-averages of the escape and precipitation rates. The precipitation
 335 rates are determined by counting macroparticles that hit the inner boundary, which in
 336 the analyzed runs is close to the exobase, and are removed from the simulation. The es-
 337 cape rates are determined as the difference between the injection rate and the precip-
 338 itation rate of a population.

339 It can be seen that the solar wind proton precipitation fluctuates close to the ULF
 340 period of 83 s. Moreover, also the ionospheric atomic and molecular oxygen ions and the
 341 exospheric photoion protons show fluctuations close to the period of 83 s. The peak-to-
 342 peak amplitude of the fluctuations is less than 5%. The solar wind alphas and the exo-
 343 spheric oxygen ions do not show such clear fluctuations.

344 4 Discussion

345 We show that a vast ion foreshock is created under radial IMF conditions (6° spi-
 346 ral angle) in a global Mars hybrid simulation. Under nominal IMF and solar minimum
 347 conditions (57° spiral angle) no proper foreshock forms and no large-scale ULF waves
 348 are excited near Mars (Figs. 1 and 2). On the other hand, the flow-aligned IMF results
 349 in a large portion of the bow shock being in the quasi-parallel regime allowing ion scat-
 350 tering and backstreaming already in the subsolar upstream region. In the foreshock, large-
 351 scale ULF waves are excited and form two distinct regions on the $z = 0$ plane (Fig. 7):
 352 the near region and the far region. The wave periods of 71-83 s dominate the near re-
 353 gion, whereas the periods of 25-28 s are found in the far region. As a comparison, the
 354 upstream ion gyro periods are from 20 s (H^+) to 631 s (O_2^+). The foreshock ULF wave
 355 period in the far region is just above the proton gyro motion and below the alpha gyro
 356 motion. In the near region, the ULF wave period is clearly above the proton and alpha
 357 gyro motion but still below the oxygen gyro motion. The period of the foreshock ULF

358 waves based on earlier empirical model are in the range of 38-56 s for the upstream conditions
 359 in the radial IMF run (*Hoppe and Russell, 1982; Le and Russell, 1996; Romanelli, DiBraccio, Gershman, Le, Mazelle, Meziane, Boardsen, Slavin, Raines, Glass, and Espley, 2020; Takahashi, McPherron, and Terasawa, 1984*). These are in the range of the
 360 periods occurring in our model. It should be noted that such empirical formulae assume
 361 a single, fixed angle between the bow shock surface normal and the IMF, whereas in reality
 362 and in our global hybrid model the ion scattering at the quasi-parallel bow shock
 363 occurs over a range of angles.
 364
 365

366 The suprathermal foreshock ions are clearly identified in the ion velocity distributions
 367 and their properties differ substantially from the incident solar wind core population (Fig. 10
 368 and Table 2). It is evident that the suprathermal beam is backstreaming with respect to the
 369 core and has a much higher temperature perpendicular to the magnetic field compared to the
 370 parallel temperature. The backstreaming part of the velocity space reaches over 10% of total
 371 solar wind proton density in the subsolar foreshock near the boundary of the ion foreshock,
 372 whereas in the far region the backstreaming proton density is only few percent or below. There
 373 are only sporadic backstreaming solar wind alphas in the foreshock. Specifically, the
 374 suprathermal solar wind proton densities are 9% at P1 in the near region and 0.7% at P4 in
 375 the far region of the core. These are typical features of the terrestrial foreshock ion
 376 populations and the morphology of the suprathermal populations in Fig. 10 qualitatively
 377 resemble the field-aligned beam and intermediate ion distributions at Earth (e.g. reviews by
 378 *Burgess, Möbius, and Scholer, 2012; Eastwood et al., 2005; Fuselier, 1994*, and references therein).
 379 The intermediate distributions are often associated with large-scale foreshock ULF waves
 380 (*Fuselier, Thomsen, Gosling, Bame, and Russell, 1986; Hoppe, Russell, Frank, Eastman, and Greenstadt, 1981; Paschmann, Sckopke, Papamastorakis, Asbridge, Bame, and Gosling, 1981*).

383 Let us now investigate how strong are the ULF waves in different regions. The peak-to-peak
 384 relative magnitude of the ULF waves is about $dB/B = 0.3$ in the upstream subsolar foreshock
 385 (P1), and it increases up to $dB/B = 1.0$ in the subsolar magnetosheath (P2). This increase
 386 is due to the plasma and magnetic field compression at the bow shock and in the magnetic
 387 barrier as also seen in the observations (*Collinson et al., 2018; Fowler et al., 2018*).
 388 In the heavy ion plume, the magnitude is damped down to $dB/B = 0.2$ (P3) due to the waves
 389 propagating into plasma with increasing mass density but approximately constant magnetic
 390 pressure. The peak-to-peak relative magnitude of the solar wind proton (alpha) ULF
 391 fluctuation is about $dn/n = 0.6$ (1.3) at P1, which is compressed to $dn/n = 3.3$ (6.7) at P2.
 392 At P3, the magnitude is damped down to $dn/n < 0.2$ (0.5). The fluctuations are visible
 393 in the bulk density but also in the omni-directional time-energy spectra. The absolute
 394 wave amplitudes are stronger in the far region than in the near region as can be seen in
 395 the time series in Figs. 4-5, which is likely associated with backstreaming ion populations
 396 having longer time to interact with the incident solar wind flow via ion-ion instabilities
 397 and excite larger amplitude ULF waves (*Gary, 1991*).

399 Next we estimate the wave length and the velocity of the ULF wave phases as follows
 400 (*Jarvinen et al., 2020b*). First, the magnetic field components are interpolated in a
 401 snapshot solution ($t = 560.4$ s) along a $4R_M$ long straight line in the wave propagation
 402 direction \hat{k} centered at the near and far region points where the MVA was performed
 403 (Fig. 4). Then the wave lengths (λ_w) are estimated from the interpolated B_i and B_j
 404 components of the MVA. Finally, the wave length and the period (τ_w) are combined to
 405 arrive at the phase speed $v_p = \lambda_w/\tau_w$. The wave length estimate in the near region is
 406 3800-5800 km (22-34 grid cells) and 6400-6900 km (38-41 grid cells) in the far region. As
 407 a comparison, only oxygen species have the gyro radius of the same order of magnitude
 408 than the wave length of the foreshock ULF waves. The phase speed along \hat{k} is estimate
 409 as 46-70 km/s in the near region and 230-246 km/s in the far region in the simulation
 410 frame. These are close to the solar wind bulk velocity projected along \hat{k} , which actually

411 fluctuates above and below the phase speed due to variations caused by the foreshock
 412 and plasma thermal motion. Thus, the phase speed estimate is not conclusive to decide
 413 whether the waves are intrinsically left-handed or right-handed in the plasma frame.

414 However, the correlation of the plasma density and the magnitude of the magnetic
 415 field is mostly strongly positive throughout the foreshock suggesting that the ULF waves
 416 are the fast magnetosonic mode in both foreshock regions (Fig. 7b). In the near region,
 417 the propagation is nearly perpendicular to the magnetic field and the polarization is highly
 418 elliptical with no clear handedness in the simulation frame due to fluctuations in the bulk
 419 velocity as discussed in the previous paragraph. On the other hand, the propagation angle
 420 of the waves is oblique with respect to the magnetic field (20-50°) and the polariza-
 421 tion is consistently left-handed and circular in the simulation frame in the far region. This
 422 is what is expected from the right-handed ion-ion instability propagating upstream in
 423 the plasma frame, but convecting downstream with the solar wind flow in the simula-
 424 tion or spacecraft frame (*Gary, 1991*).

425 As can be seen in Fig. 14, the ion pickup is highly perpendicular to the undisturbed
 426 solar wind flow ($U_x \ll U_{yz}$) as expected under a strongly flow-aligned IMF. That is,
 427 the $E \times B$ drift is highly perpendicular to the flow (Fig. 3) and the kinetic energy of
 428 pickup ions is much lower than under a nominal IMF (*Jarvinen and Kallio, 2014*). Fur-
 429 ther, large-scale planetary ion acceleration is modulated by the ULF waves as found also
 430 for Venus in our previous global hybrid modeling study (*Jarvinen et al., 2020a*). This
 431 can be seen in the dayside exospheric H_{exo}^+ and O_{exo}^+ photoion density fluctuations (Figs.
 432 11i and 12i,k). Further, the ionospheric O_{iono}^+ and $O_{2,\text{iono}}^+$ densities show sharp mod-
 433 ulations in concert with the arrival of the steepened ULF waves (Figs. 13e,g) in the heavy
 434 ion plume. This creates the periodic structures, or "vortices", in the time-energy spec-
 435 trograms of ionospheric oxygen ion populations (Figs. 13 and 14). The velocity increase
 436 associated with the "vortices" is towards the $+E_{\text{sw}}$ hemisphere (increase in U_z) and the
 437 foreshock hemisphere (decrease in U_y). This ULF modulation of the heavy ion plume
 438 can be seen as periodically fluctuating density filaments and embedded oxygen ion bursts
 439 in the supplementary material Movie S03. The bursts originate from low-altitudes near
 440 the inner boundary of the model and travel upwards resulting in the oxygen ion time-
 441 energy spectrogram vortices and density spikes. On the other hand, the periodic move-
 442 ment of the oxygen ion density filaments is associated with the wave-like behaviour in the
 443 time-energy spectrogram between the vortices. This way, the ULF waves propagate
 444 in the heavy ion plume and locally detach oxygen ion bursts or clouds near the model's
 445 inner boundary. Recently, spacecraft observations of planetary ion heating by wave-particle
 446 interactions with the steepened magnetosonic ULF waves originating from the foreshock
 447 and extending from the dayside to the nightside and down to the exobase altitude was
 448 reported at Mars (*Fowler, Hanley, McFadden, Chaston, Bonnell, Halekas, Espley, Di-*
 449 *Braccio, Schwartz, Mazelle, Mitchell, Xu, and Lillis, 2021*).

450 Note that the ion density and velocity maxima do not exactly coincide with the
 451 magnetic field maxima in Fig. 14. This is not completely unexpected as the ion motion
 452 is affected by the electric and magnetic fields (the Lorentz force) integrated along the
 453 ion trajectory rather than purely local fields. Point P3 is located 3068 km above the model's
 454 inner boundary. This means that the escaping ionospheric oxygen ions had at least sev-
 455 eral tens of seconds of time to interact with the electric and magnetic fields associated
 456 with the ULF wavefronts before reaching P3 after emission from the inner boundary. At
 457 the lowest altitudes where the oxygen energies are below 10 eV the ions can stay one or
 458 few ULF wave periods within a single simulation cell. According to *in situ* observations
 459 by the Mars Atmosphere and Volatile EvolutionN (MAVEN) orbiter the wave lengths of
 460 the ULF waves compress from thousands of kilometers at the bow shock to hundreds of
 461 kilometers in the upper Martian ionosphere (*Fowler et al., 2021*). As a comparison, the
 462 simulation grid cell size is 169.5 km in this study, and a predetermined upwards emis-
 463 sion of the ionospheric ions is used near the inner boundary rather than a more self-consistent

464 description of the ionospheric photochemistry (e.g. *Brecht, Ledvina, and Bougher, 2016;*
 465 *Ledvina, Brecht, Brain, and Jakosky, 2017; Modolo et al., 2016*). Finite grid cell size re-
 466 sults also in "reverse energy-time dispersed" signatures of H_{EXO}^+ and O_{EXO}^+ spectra at $\lesssim 100$
 467 eV energies in Figs. 11-13. A dispersion signature is created when a single macropar-
 468 ticle is accelerated and gains energy within a grid cell. Even though our results demon-
 469 strate the connection between the foreshock ULF waves transmitted downstream and
 470 the modulation of the planetary heavy ion escape, more detailed simulations are needed
 471 to fully resolve the scales of the ULF wave - ionospheric ion interactions at the lowest
 472 altitudes.

473 Another important question is how the local ion escape is affected by the ULF waves
 474 in the heavy ion plume? The order of magnitude of the density variation is over 100 for
 475 O_2^+ and over 10 for O^+ at P3 (Fig. 12), which can also be seen on the $+E_{\text{SW}}$ hemisphere
 476 in the upper xz and yz panels of Movie S02 and Movie S03 (supplementary material).
 477 Moreover, the local bulk escape flux varies more than two orders of magnitude for these
 478 populations. Thus, the ULF waves modulate the heavy ion plume and planetary ion ac-
 479 celeration very strongly locally. Strong local variations (more than two orders of mag-
 480 nitude with respect to the mean value) in the heavy ion escape have also been observed
 481 by MAVEN and occur often in the $+E_{\text{SW}}$ hemisphere (*Dubinin et al., 2021*). It was pro-
 482 posed that is related to waves and instabilities.

483 Even though the local oxygen ion escape flux can increase more than two orders
 484 of magnitude in concert with the ULF wavefront, the integrated global escape rate is mod-
 485 ulated only by few percents or less (Fig. 15). This can be understood such that, even
 486 though the ULF waves modify the morphology of the heavy ion plume locally rather strongly,
 487 their modulation effect on the global ion escape is smoothed out by mixing of the dif-
 488 ferent wave phases in the simulation domain. What is left in global scale is the average
 489 effect of the wave-particle interactions.

490 We speculate that the presence of crustal magnetic anomalies, which are not in-
 491 cluded in our current simulation runs, may play a role in the interaction between the ULF
 492 waves and the Martian ion escape. Specifically, is there a connection between the ob-
 493 served episodic bulk plasma escape bursts (*Brain, Baker, Briggs, Eastwood, Halekas, and*
 494 *Phan, 2010b; Fang, Ma, Masunaga, Dong, Brain, Halekas, Lillis, Jakosky, Connerney,*
 495 *Grebowsky, and Dong, 2017*) and the foreshock ULF waves? The interplay of crustal mag-
 496 netic fields and plasma waves in the Mars induced magnetosphere should be analyzed
 497 in future studies.

498 We emphasize that it is essential to take into account global context when analyz-
 499 ing *in situ* observation of planetary ion escape and, especially, waves and other spatio-
 500 temporal phenomena.

501 As a comparison, the foreshock ULF waves modulate the solar wind induced ion
 502 escape from Venus by 25% under nominal conditions in our earlier global hybrid mod-
 503 eling study (*Jarvinen et al., 2020a*). This is much stronger than a few percent at Mars
 504 found in this study. We attribute the difference to the denser solar wind and stronger
 505 IMF and, thus, stronger ULF waves at Venus. The nature of the ULF wave modulation
 506 of the planetary ion acceleration and plasma environment at Mars and Venus should be
 507 a topic for more detailed comparative studies using a range of upstream parameter cases
 508 at both planets.

509 Another difference between the foreshocks of Mars and Venus in a global hybrid
 510 simulation is the two ULF wave regions at Mars. The ULF modulation of the ion escape
 511 occurs at about the same period than the ULF waves in the near foreshock region (the
 512 83-s waves). This is expected as the near region waves propagate towards the planet and
 513 the low-altitude, high-density regions where the initial planetary ion acceleration takes
 514 place. In the far region, the planetary ions have already reached high energies and their

515 dynamics may not couple as efficiently with the ULF waves as in the near region. Also,
 516 the wave lengths in the far region are larger than the ion gyro radii of all ion species in
 517 the analyzed upstream condition case. However, the excitation and interplay of the ULF
 518 waves and the ion velocity distributions in the two foreshock regions should be a topic
 519 in a detailed study.

520 Table 3 lists the global escape rates of the planetary ion populations from the sim-
 521 ulation domain, the precipitation rates of all ion populations to the inner boundary and
 522 the ratio of the escape rate to the injection rate per population for both runs. See Fig.
 523 15 (Fig. S04 in the supplementary material) for time series of precipitation and escape
 524 rates in the radial IMF (nominal) run. The sum of the escape rate and the precipita-
 525 tion rate of an injected planetary ion population equal to the injection rate. The escape
 526 rates of ionospheric populations are enhanced by 74% (O_{iono}^+) and 64% ($O_{2,\text{iono}}^+$) in the
 527 radial IMF run compared to the nominal run. The increase in the ionospheric escape from
 528 an unmagnetized planet under a flow-aligned IMF has been associated with a change in
 529 the magnetic morphology of the induced magnetosphere and a disappearance of a well-
 530 developed magnetic barrier (Liu, Kallio, Jarvinen, Lammer, Lichtenegger, Kulikov, Ter-
 531 ada, Zhang, and Janhunen, 2009; Zhang, Du, Ma, Lammer, Baumjohann, Wang, and
 532 Russell, 2009). Moreover, even though the escape rates increases, the pickup ion energy
 533 becomes lower the more radial the IMF is due to the projection of the $E \times B$ velocity with
 534 respect to the solar wind flow (Jarvinen and Kallio, 2014). The gyroaveraged energy of
 535 a scatter-free pickup O^+ ion is 0.33 keV in the upstream solar wind in the radial IMF
 536 run and 22 keV in the nominal run, whereas the kinetic energy of an O^+ ion moving at
 537 the Mars escape velocity (5.03 km/s) is only 2.1 eV.

538 The exospheric photoion escape does not change considerably between our two runs.
 539 This is due to the fact that 80-90% of the created exospheric ions escape in both cases
 540 anyway, i.e. the exospheric photoion escape is almost saturated or production limited
 541 (Ramstad, Barabash, Futaana, Nilsson, and Holmström, 2017). On the other hand, the
 542 ionospheric escape is more limited by acceleration processes or available momentum and
 543 energy and show a greater difference between the two runs. The obtained heavy ion es-
 544 cape rates are well within the estimates based on *in situ* spacecraft observations, which
 545 range from about the order of magnitude of 10^{24} to 10^{25} particles per second (see Du-
 546 binin et al., 2011; Jakosky, Brain, Chaffin, Curry, Deighan, Grebowsky, Halekas, Leblanc,
 547 Lillis, Luhmann, Andersson, Andre, Andrews, Baird, Baker, Bell, Benna, Bhattacharyya,
 548 Bougher, Bowers, Chamberlin, Chaufray, Clarke, Collinson, Combi, Connerney, Con-
 549 nour, Correira, Crabb, Crary, Cravens, Crismani, Delory, Dewey, DiBraccio, Dong, Dong,
 550 Dunn, Egan, Elrod, England, Eparvier, Ergun, Eriksson, Esman, Espley, Evans, Fallows,
 551 Fang, Fillingim, Flynn, Fogle, Fowler, Fox, Fujimoto, Garnier, Girazian, Groeller, Grues-
 552 beck, Hamil, Hanley, Hara, Harada, Hermann, Holmberg, Holsclaw, Houston, Inui, Jain,
 553 Jolitz, Kotova, Kuroda, Larson, Lee, Lee, Lefevre, Lentz, Lo, Lugo, Ma, Mahaffy, Mar-
 554 quette, Matsumoto, Mayyasi, Mazelle, McClintock, McFadden, Medvedev, Mendillo, Meziane,
 555 Milby, Mitchell, Modolo, Montmessin, Nagy, Nakagawa, Narvaez, Olsen, Pawlowski, Pe-
 556 terson, Rahmati, Roeten, Romanelli, Ruhunusiri, Russell, Sakai, Schneider, Seki, Shar-
 557 rar, Shaver, Siskind, Slipki, Soobiah, Steckiewicz, Stevens, Stewart, Stiepen, Stone, Ten-
 558 ishev, Terada, Terada, Thiemann, Tolson, Toth, Trovato, Vogt, Weber, Withers, Xu, Yelle,
 559 Yigit, and Zurek, 2018, and references therein).

560 We find that the ULF waves also modulate the solar wind proton flux precipitat-
 561 ing in the model's inner boundary near the exobase. The magnitude of this modulation
 562 is a few percent of the total precipitation flux (Fig. 15). The alpha precipitation is not
 563 clearly affected by the ULF waves. This is likely due to longer He^{++} gyro radius (up-
 564 stream: 229 km) compared to H^+ (upstream: 123 km). That is, the motion of alphas
 565 is more rigid compared to protons, and alphas can "jump" over the weak magnetic bar-
 566 rier whereas protons are more magnetized and can feel the local ULF modulations as they
 567 are intensified in the region. The mean total solar wind H_{SW}^+ (He_{SW}^{++}) precipitation rate

568 under the radial IMF is 8.3 (6.8) times the value under the nominal IMF (Table 3). The
 569 increase is associated with the flow-aligned IMF opening a magnetic connection from the
 570 solar wind to the dayside inner boundary and in the same time the perpendicular IMF
 571 component is weak meaning that the pile up of the magnetic field and the creation of
 572 a proper magnetic barrier does not occur (*Zhang et al.*, 2009). Together these allow the
 573 solar wind almost a direct entry to the inner boundary. The effect of the ULF wave mod-
 574 ulation on the sputtering related escape at Mars (e.g. *Martinez, Modolo, Leblanc, Chaufray,*
 575 *Witasse, Romanelli, Dong, Hara, Halekas, Lillis, McFadden, Eparvier, Leclercq, Luh-*
 576 *mann, Curry, and Jakosky*, 2020, and references therein) should be investigated in fu-
 577 ture studies.

578 5 Conclusions

579 We have analyzed the solar wind interaction with Mars in a global three-dimensional
 580 hybrid simulation. We find a well-developed ion foreshock under strongly radial IMF but
 581 otherwise nominal upstream solar wind conditions and solar minimum photon flux. We
 582 identify two distinct foreshock regions with fast magnetosonic ULF waves: the near re-
 583 gion where the wave period is 71-83 s and the far region where the wave period is 25-
 584 28 s. The waves in the near region transmit downstream through the bow shock and af-
 585 fect dynamics of solar wind and planetary ions. Ion precipitation rates into the exobase
 586 and planetary ion escape rates show upto few percent peak-to-peak modulations at the
 587 ULF wave period corresponding to the near foreshock region. Ionospheric oxygen ion es-
 588 cape fluxes show more than two orders of magnitude local modulations in the heavy plume
 589 at the same period. Finally, the escape rates of the ionospheric oxygen ion populations
 590 are enhanced by 60-70% under radial IMF conditions compared to nominal upstream con-
 591 ditions.

673 Acknowledgments

674 The work was supported by the Academy of Finland (Decision No. 310444). The au-
 675 thors thank the ISSI (International Space Science Institute) and ISSI-BJ (International
 676 Space Science Institute Beijing) team “Dayside Transient Phenomena and Their Impact
 677 on the Magnetosphere-Ionosphere” for discussions and suggestions. Figures 1-3 were cre-
 678 ated using the VisIt open-source visualisation tool (*Childs, Brugger, Whitlock, Mered-*
 679 *ith, Ahern, Pugmire, Biagas, Müller, Harrison, Weber, Krishnan, Fogal, Sanderson, Garth,*
 680 *Bethel, Camp, Rübel, Durant, Favre, and Navrátil*, 2012). We acknowledge the compu-
 681 tational resources provided by the Aalto Science-IT project. Global three-dimensional
 682 hybrid simulations were performed using the RHybrid simulation platform, which is avail-
 683 able under an open-source license by the Finnish Meteorological Institute ([https://github](https://github.com/fmihpc/rhybrid/)
 684 [.com/fmihpc/rhybrid/](https://github.com/fmihpc/rhybrid/)). The simulation code version used in this study is archived (un-
 685 der DOI: 10.5281/zenodo.6185399).

686 6 References

687 References

- 688 Bertucci, C., N. Romanelli, J. Y. Chaufray, D. Gomez, C. Mazelle, M. Delva,
 689 R. Modolo, F. González-Galindo, and D. A. Brain (2013), Temporal vari-
 690 ability of waves at the proton cyclotron frequency upstream from Mars: Im-
 691 plications for Mars distant hydrogen exosphere, *Geophys. Res. Lett.*, *40*(15),
 692 3809–3813, 10.1002/grl.50709.
- 693 Bougher, S. W., P.-L. Blelly, M. Combi, J. L. Fox, I. Mueller-Wodarg, A. Ridley,
 694 and R. G. Roble (2008), Neutral Upper Atmosphere and Ionosphere Modeling,
 695 *Space Sci. Rev.*, *139*(1-4), 107–141, 10.1007/s11214-008-9401-9.
- 696 Brain, D., S. Barabash, A. Boesswetter, S. Bougher, S. Brecht, G. Chanteur,

592

Table 1. Global hybrid model setup and undisturbed upstream solar wind (SW) and interplanetary magnetic field (IMF) conditions.

593

Parameter	Value
Box size ($x \times y \times z$) [R_M]	$(-5\dots 10) \times (-10\dots 3) \times (-3\dots 3)$
Number of grid cells ($n_x \times n_y \times n_z$)	$300 \times 260 \times 120$
Grid cell size (Δx)	$(169.5 \text{ km})^3 = (R_M/20)^3$
Timestep (Δt)	11.2 ms
SW bulk velocity vector [v_x, v_y, v_z]	$[-430, 0, 0]$ km/s
H _{sw} ⁺ temperature	6.1×10^4 K
He _{sw} ⁺⁺ temperature	21.35×10^4 K
H _{sw} ⁺ density	3 cm^{-3}
He _{sw} ⁺⁺ density	0.12 cm^{-3}
Electron temperature	10^4 K
Run 1: IMF vector [B_x, B_y, B_z]	$[-3.28, 0.344, 0]$ nT
Run 1: IMF spiral angle	6° (away sector)
Run 2: IMF vector [B_x, B_y, B_z]	$[-1.797, 2.768, 0]$ nT
Run 2: IMF spiral angle	57° (away sector)
IMF magnitude	3.3 nT
Alfvén Mach number	11.1
Sonic Mach number	8.6
Magnetosonic Mach number	6.8
Plasma beta	1.7
Superconducting shell radius (R_η)	3690 km = $R_M + 300$ km
Obstacle resistivity ($r < R_\eta$)	0
Plasma resistivity ($r \geq R_\eta$)	$8.92 \times 10^{-3} \times \mu_0 \Delta x^2 / \Delta t$
Particle absorption radius	3590 km = $R_M + 200$ km
H _{exo} ⁺ photoion prod. rate	$2.15 \times 10^{24} \text{ s}^{-1}$
O _{exo} ⁺ photoion prod. rate	$2.67 \times 10^{23} \text{ s}^{-1}$
O _{iono} ⁺ ionospheric emis. rate	$1.4 \times 10^{25} \text{ s}^{-1}$
O _{2,iono} ⁺ ionospheric emis. rate	$2.0 \times 10^{25} \text{ s}^{-1}$
Ionospheric emis. radius	$R_M + 400$ km
Solar EUV photo rates	solar minimum

594

Table 2. Bulk properties of the incident core and suprathermal foreshock H_{sw}⁺ populations shown in Fig. 10. The bulk velocity is given in the simulation frame.

595

Region / Population	Density [cm^{-3}]	Temperature [10^4 K]	Bulk velocity [km/s]
Near (P1)			
/Core	2.76	6.1	$[-428, 18, -1]$
/Suprathermal	0.25	431.2	$[262, 0, -77]$
Far (P4)			
/Core	2.84	6.1	$[-430, -3, 4]$
/Suprathermal	0.02	282.2	$[-53, -120, -25]$

596
597**Table 3.** Global temporal average ion escape and precipitation rates and the ratio of the escape rate to the injection rate of planetary ion populations.

Population	Precipitation rate [10^{24} s^{-1}]	Escape rate [10^{24} s^{-1}]	Escape/inject
Run 1			
H_{sw}^+	30.4	-	-
$\text{He}_{\text{sw}}^{++}$	1.6	-	-
O_{iono}^+	8.6	5.4	0.39
$\text{O}_{2,\text{iono}}^+$	11.8	8.2	0.41
H_{exo}^+	0.25	1.9	0.88
O_{exo}^+	0.03	0.23	0.88
Run 2			
H_{sw}^+	3.6	-	-
$\text{He}_{\text{sw}}^{++}$	0.24	-	-
O_{iono}^+	10.9	3.1	0.22
$\text{O}_{2,\text{iono}}^+$	15.0	5.0	0.25
H_{exo}^+	0.12	2.0	0.94
O_{exo}^+	0.05	0.22	0.82

697
698
699
700
701
702
703
704
705
706
707
708
709
710
711
712
713
714
715
716
717
718
719
720
721
722
723
724
725

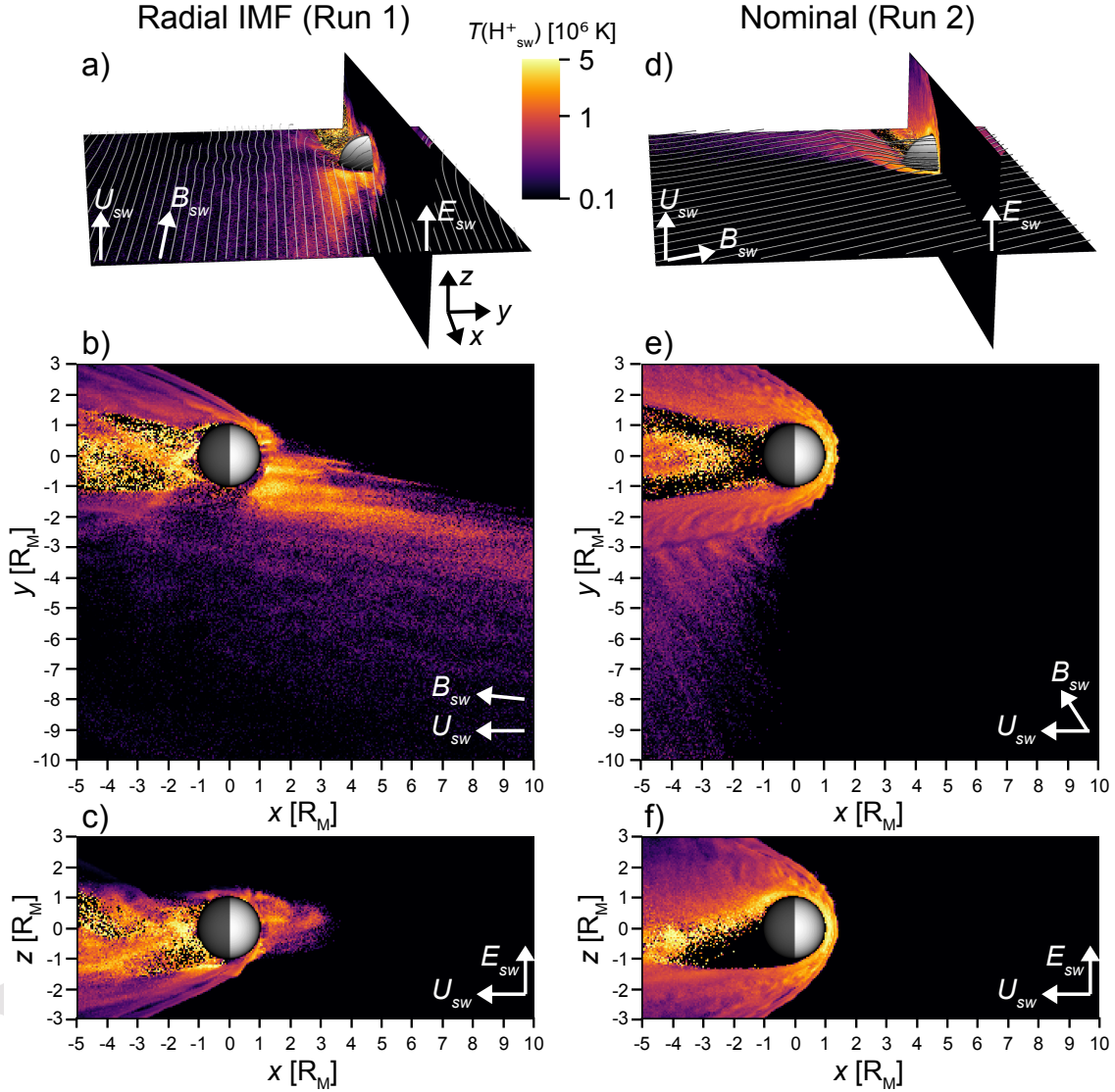
- D. Hurley, E. Dubinin, X. Fang, M. Fraenz, J. Halekas, E. Harnett, M. Holmstrom, E. Kallio, H. Lammer, S. Ledvina, M. Liemohn, K. Liu, J. Luhmann, Y. Ma, R. Modolo, A. Nagy, U. Motschmann, H. Nilsson, H. Shinagawa, S. Simon, and N. Terada (2010a), A comparison of global models for the solar wind interaction with Mars, *Icarus*, *206*, 139–151, 10.1016/j.icarus.2009.06.030.
- Brain, D. A., F. Bagenal, M. H. Acuña, J. E. P. Connerney, D. H. Crider, C. Mazelle, D. L. Mitchell, and N. F. Ness (2002), Observations of low-frequency electromagnetic plasma waves upstream from the Martian shock, *J. Geophys. Res.*, *107*(A6), 1076, 10.1029/2000JA000416.
- Brain, D. A., A. H. Baker, J. Briggs, J. P. Eastwood, J. S. Halekas, and T.-D. Phan (2010b), Episodic detachment of Martian crustal magnetic fields leading to bulk atmospheric plasma escape, *Geophys. Res. Lett.*, *37*, L14108, 10.1029/2010GL043916.
- Brain, D. A., F. Bagenal, Y. J. Ma, H. Nilsson, and G. Stenberg Wieser (2016), Atmospheric escape from unmagnetized bodies, *J. Geophys. Res.*, *121*(12), 2364–2385, 10.1002/2016JE005162.
- Brecht, S. H., S. A. Ledvina, and S. W. Bougher (2016), Ionospheric loss from Mars as predicted by hybrid particle simulations, *J. Geophys. Res.*, *121*(10), 10,190–10,208, 10.1002/2016JA022548.
- Burgess, D., E. Möbius, and M. Scholer (2012), Ion Acceleration at the Earth’s Bow Shock, *Space Sci. Rev.*, *173*, 5–47, 10.1007/s11214-012-9901-5.
- Chaffin, M. S., J.-Y. Chaufray, I. Stewart, F. Montmessin, N. M. Schneider, and J.-L. Bertaux (2014), Unexpected variability of Martian hydrogen escape, *Geophys. Res. Lett.*, *41*, 314–320, 10.1002/2013GL058578.
- Childs, H., E. Brugger, B. Whitlock, J. Meredith, S. Ahern, D. Pugmire, K. Biagas, M. Miller, C. Harrison, G. H. Weber, H. Krishnan, T. Fogal, A. Sanderson, C. Garth, E. W. Bethel, D. Camp, O. Rübél, M. Durant, J. M. Favre, and P. Navrátil (2012), VisIt: An End-User Tool For Visualizing and Analyzing Very Large Data, in *High Performance Visualization—Enabling Extreme-Scale*

- 726 *Scientific Insight*, pp. 357–372, CRC Press, New York.
- 727 Collinson, G., L. B. Wilson, N. Omidi, D. Sibeck, J. Espley, C. M. Fowler,
- 728 D. Mitchell, J. Grebowsky, C. Mazelle, S. Ruhunusiri, J. Halekas, R. Frahm,
- 729 T. Zhang, Y. Futaana, and B. Jakosky (2018), Solar Wind Induced Waves in
- 730 the Skies of Mars: Ionospheric Compression, Energization, and Escape Result-
- 731 ing From the Impact of Ultralow Frequency Magnetosonic Waves Generated
- 732 Upstream of the Martian Bow Shock, *J. Geophys. Res.*, *123*(9), 7241–7256,
- 733 10.1029/2018JA025414.
- 734 Delva, M., and E. Dubinin (1998), Upstream ULF fluctuations near Mars, *J. Geo-*
- 735 *phys. Res.*, *103*(A1), 317–326, 10.1029/97JA02501.
- 736 Dong, Y., X. Fang, D. A. Brain, J. P. McFadden, J. S. Halekas, J. E. P. Connerney,
- 737 F. Eparvier, L. Andersson, D. Mitchell, and B. M. Jakosky (2017), Seasonal
- 738 variability of Martian ion escape through the plume and tail from MAVEN
- 739 observations, *J. Geophys. Res.*, *122*(4), 4009–4022, 10.1002/2016JA023517.
- 740 Dubinin, E., and M. Fraenz (2016), Ultra-Low-Frequency Waves at Venus and Mars,
- 741 *Washington DC American Geophysical Union Geophysical Monograph Series*,
- 742 *216*, 343–364, 10.1002/9781119055006.ch20.
- 743 Dubinin, E., M. Fraenz, A. Fedorov, R. Lundin, N. Edberg, F. Duru, and O. Vais-
- 744 berg (2011), Ion Energization and Escape on Mars and Venus, *Space Sci. Rev.*,
- 745 *162*, 173–211, 10.1007/s11214-011-9831-7.
- 746 Dubinin, E., M. Fraenz, M. Pätzold, S. Tellmann, J. Woch, J. McFadden, and L. Ze-
- 747 lenyi (2021), Bursty Ion Escape Fluxes at Mars, *J. Geophys. Res.*, *126*(4),
- 748 e28920, 10.1029/2020JA028920.
- 749 Eastwood, J. P., E. A. Lucek, C. Mazelle, K. Meziane, Y. Narita, J. Pickett,
- 750 and R. A. Treumann (2005), The Foreshock, *Space Sci. Rev.*, *118*, 41–94,
- 751 10.1007/s11214-005-3824-3.
- 752 Egan, H., Y. Ma, C. Dong, R. Modolo, R. Jarvinen, S. Bougher, J. Halekas,
- 753 D. Brain, J. Mcfadden, J. Connerney, D. Mitchell, and B. Jakosky (2018),
- 754 Comparison of Global Martian Plasma Models in the Context of MAVEN
- 755 Observations, *J. Geophys. Res.*, *123*, 3714–3726, 10.1029/2017JA025068.
- 756 Fang, X., Y. Ma, K. Masunaga, Y. Dong, D. Brain, J. Halekas, R. Lillis, B. Jakosky,
- 757 J. Connerney, J. Grebowsky, and C. Dong (2017), The Mars crustal magnetic
- 758 field control of plasma boundary locations and atmospheric loss: MHD pre-
- 759 diction and comparison with MAVEN, *J. Geophys. Res.*, *122*(4), 4117–4137,
- 760 10.1002/2016JA023509.
- 761 Fowler, C. M., L. Andersson, R. E. Ergun, Y. Harada, T. Hara, G. Collinson, W. K.
- 762 Peterson, J. Espley, J. Halekas, J. Mcfadden, D. L. Mitchell, C. Mazelle,
- 763 M. Benna, and B. M. Jakosky (2018), MAVEN Observations of Solar Wind-
- 764 Driven Magnetosonic Waves Heating the Martian Dayside Ionosphere, *J. Geo-*
- 765 *phys. Res.*, *123*(5), 4129–4149, 10.1029/2018JA025208.
- 766 Fowler, C. M., J. Halekas, S. Schwartz, K. A. Goodrich, J. R. Gruesbeck, and
- 767 M. Benna (2019), The Modulation of Solar Wind Hydrogen Deposition in
- 768 the Martian Atmosphere by Foreshock Phenomena, *J. Geophys. Res.*, *124*(8),
- 769 7086–7097, 10.1029/2019JA026938.
- 770 Fowler, C. M., K. G. Hanley, J. P. McFadden, C. C. Chaston, J. W. Bonnell,
- 771 J. S. Halekas, J. R. Espley, G. A. DiBraccio, S. J. Schwartz, C. Mazelle,
- 772 D. L. Mitchell, S. Xu, and R. J. Lillis (2021), MAVEN Observations of
- 773 Low Frequency Steepened Magnetosonic Waves and Associated Heating
- 774 of the Martian Nightside Ionosphere, *J. Geophys. Res.*, *126*(10), e29615,
- 775 10.1029/2021JA029615.
- 776 Fuselier, S. A. (1994), Suprathermal ions upstream and downstream from the
- 777 Earth’s bow shock, *Washington DC American Geophysical Union Geophys-*
- 778 *ical Monograph Series*, *81*, 107–119, 10.1029/GM081p0107.
- 779 Fuselier, S. A., M. F. Thomsen, J. T. Gosling, S. J. Bame, and C. T. Russell (1986),
- 780 Gyrating and intermediate ion distributions upstream from the earth’s bow

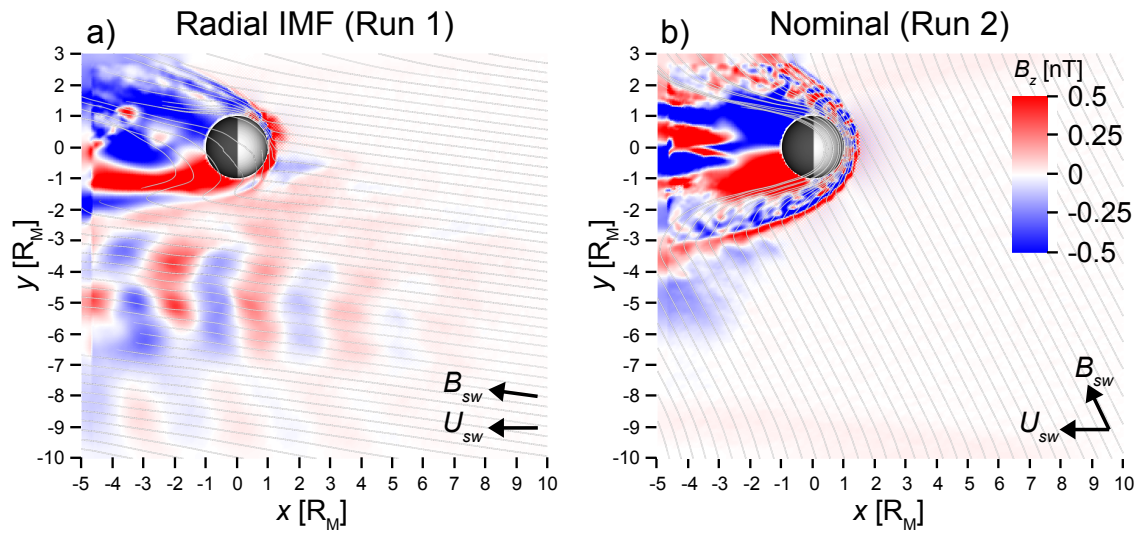
- 781 shock, *J. Geophys. Res.*, *91*, 91–99, 10.1029/JA091iA01p00091.
- 782 Futaana, Y., G. Stenberg Wieser, S. Barabash, and J. G. Luhmann (2017), Solar
783 Wind Interaction and Impact on the Venus Atmosphere, *Space Sci. Rev.*,
784 *212*(3-4), 1453–1509, 10.1007/s11214-017-0362-8.
- 785 Gary, S. P. (1991), Electromagnetic ion/ion instabilities and their consequences in
786 space plasmas - A review, *Space Sci. Rev.*, *56*, 373–415, 10.1007/BF00196632.
- 787 Halekas, J. S., J. P. McFadden, J. E. P. Connerney, J. R. Espley, D. A. Brain, D. L.
788 Mitchell, D. E. Larson, Y. Harada, T. Hara, S. Ruhunusiri, and B. M. Jakosky
789 (2015), Time-dispersed ion signatures observed in the Martian magnetosphere
790 by MAVEN, *Geophys. Res. Lett.*, *42*(21), 8910–8916, 10.1002/2015GL064781.
- 791 Halekas, J. S., S. Ruhunusiri, Y. Harada, G. Collinson, D. L. Mitchell, C. Mazelle,
792 J. P. McFadden, J. E. P. Connerney, J. R. Espley, F. Eparvier, J. G. Luh-
793 mann, and B. M. Jakosky (2017), Structure, dynamics, and seasonal variability
794 of the Mars-solar wind interaction: MAVEN Solar Wind Ion Analyzer in-
795 flight performance and science results, *J. Geophys. Res.*, *122*(1), 547–578,
796 10.1002/2016JA023167.
- 797 Hoppe, M. M., and C. T. Russell (1982), Particle acceleration at planetary bow
798 shock waves, *Nature*, *295*, 41, 10.1038/295041a0.
- 799 Hoppe, M. M., C. T. Russell, L. A. Frank, T. E. Eastman, and E. W. Greenstadt
800 (1981), Upstream hydromagnetic waves and their association with backstream-
801 ing ion populations - ISEE 1 and 2 observations, *J. Geophys. Res.*, *86*, 4471–
802 4492, 10.1029/JA086iA06p04471.
- 803 Jakosky, B. M., D. Brain, M. Chaffin, S. Curry, J. Deighan, J. Grebowsky,
804 J. Halekas, F. Leblanc, R. Lillis, J. G. Luhmann, L. Andersson, N. An-
805 dre, D. Andrews, D. Baird, D. Baker, J. Bell, M. Benna, D. Bhat-
806 tacharyya, S. Bougher, C. Bowers, P. Chamberlin, J. Y. Chaufray, J. Clarke,
807 G. Collinson, M. Combi, J. Connerney, K. Connour, J. Correira, K. Crabb,
808 F. Crary, T. Cravens, M. Crismani, G. Delory, R. Dewey, G. DiBraccio,
809 C. Dong, Y. Dong, P. Dunn, H. Egan, M. Elrod, S. England, F. Eparvier,
810 R. Ergun, A. Eriksson, T. Esman, J. Espley, S. Evans, K. Fallows, X. Fang,
811 M. Fillingim, C. Flynn, A. Fogle, C. Fowler, J. Fox, M. Fujimoto, P. Gar-
812 nier, Z. Girazian, H. Groeller, J. Gruesbeck, O. Hamil, K. G. Hanley,
813 T. Hara, Y. Harada, J. Hermann, M. Holmberg, G. Holsclaw, S. Houston,
814 S. Inui, S. Jain, R. Jolitz, A. Kotova, T. Kuroda, D. Larson, Y. Lee, C. Lee,
815 F. Lefevre, C. Lentz, D. Lo, R. Lugo, Y. J. Ma, P. Mahaffy, M. L. Mar-
816 quette, Y. Matsumoto, M. Mayyasi, C. Mazelle, W. McClintock, J. McFadden,
817 A. Medvedev, M. Mendillo, K. Meziane, Z. Milby, D. Mitchell, R. Modolo,
818 F. Montmessin, A. Nagy, H. Nakagawa, C. Narvaez, K. Olsen, D. Pawlowski,
819 W. Peterson, A. Rahmati, K. Roeten, N. Romanelli, S. Ruhunusiri, C. Rus-
820 sell, S. Sakai, N. Schneider, K. Seki, R. Sharrar, S. Shaver, D. E. Siskind,
821 M. Slipski, Y. Soobiah, M. Steckiewicz, M. H. Stevens, I. Stewart, A. Stiepen,
822 S. Stone, V. Tennishev, N. Terada, K. Terada, E. Thiemann, R. Tolson,
823 G. Toth, J. Trovato, M. Vogt, T. Weber, P. Withers, S. Xu, R. Yelle, E. Yiğit,
824 and R. Zurek (2018), Loss of the Martian atmosphere to space: Present-day
825 loss rates determined from MAVEN observations and integrated loss through
826 time, *Icarus*, *315*, 146–157, 10.1016/j.icarus.2018.05.030.
- 827 Jarvinen, R., and E. Kallio (2014), Energization of planetary pickup ions in the solar
828 system, *J. Geophys. Res.*, *119*, 219–236, 10.1002/2013JE004534.
- 829 Jarvinen, R., E. Kallio, P. Janhunen, S. Barabash, T. L. Zhang, V. Pohjola, and
830 I. Sillanpää (2009), Oxygen ion escape from Venus in a global hybrid simula-
831 tion: role of the ionospheric O⁺ ions, *Ann. Geophys.*, *27*, 4333–4348.
- 832 Jarvinen, R., D. A. Brain, R. Modolo, A. Fedorov, and M. Holmström (2018), Oxy-
833 gen Ion Energization at Mars: Comparison of MAVEN and Mars Express
834 Observations to Global Hybrid Simulation, *J. Geophys. Res.*, *123*, 1678–1689,
835 10.1002/2017JA024884.

- 836 Jarvinen, R., M. Alho, E. Kallio, and I. Pulkkinen, Tuija (2020a), Oxygen Ion
837 Escape From Venus Is Modulated by Ultra-Low Frequency Waves, *Geo-*
838 *phys. Res. Lett.*, *47*(11), e87462, 10.1029/2020GL087462.
- 839 Jarvinen, R., M. Alho, E. Kallio, and T. I. Pulkkinen (2020b), Ultra-low-frequency
840 waves in the ion foreshock of Mercury: a global hybrid modelling study,
841 *Mon. Notices Royal Astron. Soc.*, *491*(3), 4147–4161, 10.1093/mnras/stz3257.
- 842 Kallio, E., and P. Janhunen (2002), Ion escape from Mars in a quasi-neutral hybrid
843 model, *J. Geophys. Res.*, *107*, 1035, 10.1029/2001JA000090.
- 844 Kallio, E., and P. Janhunen (2003), Modelling the solar wind interaction with Mer-
845 cury by a quasi-neutral hybrid model, *Ann. Geophys.*, *21*, 2133–2145.
- 846 Kallio, E., and R. Jarvinen (2012), Kinetic effects on ion escape at Mars and
847 Venus: Hybrid modeling studies, *Earth Planets Space*, *64*, 157–163, 10.5047/
848 eps.2011.08.014.
- 849 Kallio, E., K. Liu, R. Jarvinen, V. Pohjola, and P. Janhunen (2010), Oxygen ion
850 escape at Mars in a hybrid model: High energy and low energy ions, *Icarus*,
851 *206*, 152–163, 10.1016/j.icarus.2009.05.015.
- 852 Le, G., and C. T. Russell (1996), Solar wind control of upstream wave frequency,
853 *J. Geophys. Res.*, *101*(A2), 2571–2576, 10.1029/95JA03151.
- 854 Le, G., P. J. Chi, X. Blanco-Cano, S. Boardsen, J. A. Slavin, B. J. Anderson, and
855 H. Korth (2013), Upstream ultra-low frequency waves in Mercury’s foreshock
856 region: MESSENGER magnetic field observations, *J. Geophys. Res.*, *118*,
857 2809–2823, 10.1002/jgra.50342.
- 858 Ledvina, S. A., S. H. Brecht, D. A. Brain, and B. M. Jakosky (2017), Ion escape
859 rates from Mars: Results from hybrid simulations compared to MAVEN obser-
860 vations, *J. Geophys. Res.*, *122*, 8391–8408, 10.1002/2016JA023521.
- 861 Liu, D., Z. Rong, J. Gao, J. He, L. Klinger, M. W. Dunlop, L. Yan, K. Fan, and
862 Y. Wei (2021), Statistical Properties of Solar Wind Upstream of Mars:
863 MAVEN Observations, *ApJ*, *911*(2), 113, 10.3847/1538-4357/abed50.
- 864 Liu, K., E. Kallio, R. Jarvinen, H. Lammer, H. I. M. Lichtenegger, Y. N. Kulikov,
865 N. Terada, T. L. Zhang, and P. Janhunen (2009), Hybrid simulations of the
866 O⁺ ion escape from Venus: Influence of the solar wind density and the IMF x
867 component, *Adv. Space Res.*, *43*, 1436–1441, 10.1016/j.asr.2009.01.005.
- 868 Luhmann, J. G., C. T. Russell, J. L. Phillips, and A. Barnes (1987), On the role
869 of the quasi-parallel bow shock in ion pickup - A lesson from Venus?, *J. Geo-*
870 *phys. Res.*, *92*, 2544–2550, 10.1029/JA092iA03p02544.
- 871 Luhmann, J. G., T. Zhang, S. M. Petrinec, C. T. Russell, P. Gazis, and A. Barnes
872 (1993), Solar cycle 21 effects on the Interplanetary Magnetic Field and
873 related parameters at 0.7 and 1.0 AU, *J. Geophys. Res.*, *98*, 5559–5572,
874 10.1029/92JA02235.
- 875 Lundin, R., H. Lammer, and I. Ribas (2007), Planetary Magnetic Fields and So-
876 lar Forcing: Implications for Atmospheric Evolution, *Space Sci. Rev.*, *129*,
877 245–278, 10.1007/s11214-007-9176-4.
- 878 Lundin, R., S. Barabash, E. Dubinin, D. Winningham, and M. Yamauchi (2011),
879 Low-altitude acceleration of ionospheric ions at Mars, *Geophys. Res. Lett.*,
880 *38*(8), L08108, 10.1029/2011GL047064.
- 881 Martinez, A., R. Modolo, F. Leblanc, J. Y. Chaufray, O. Witasse, N. Romanelli,
882 Y. Dong, T. Hara, J. Halekas, R. Lillis, J. McFadden, F. Eparvier, L. Leclercq,
883 J. Luhmann, S. Curry, and B. Jakosky (2020), Influence of the Solar Wind
884 Dynamic Pressure on the Ion Precipitation: MAVEN Observations and Simula-
885 tion Results, *J. Geophys. Res.*, *125*(10), e28183, 10.1029/2020JA028183.
- 886 Mazelle, C., D. Winterhalter, K. Sauer, J. G. Trotignon, M. H. Acuña,
887 K. Baumgärtel, C. Bertucci, D. A. Brain, S. H. Brecht, M. Delva, E. Dubinin,
888 M. Øieroset, and J. Slavin (2004), Bow Shock and Upstream Phenomena at
889 Mars, *Space Sci. Rev.*, *111*(1), 115–181, 10.1023/B:SPAC.0000032717.98679.d0.

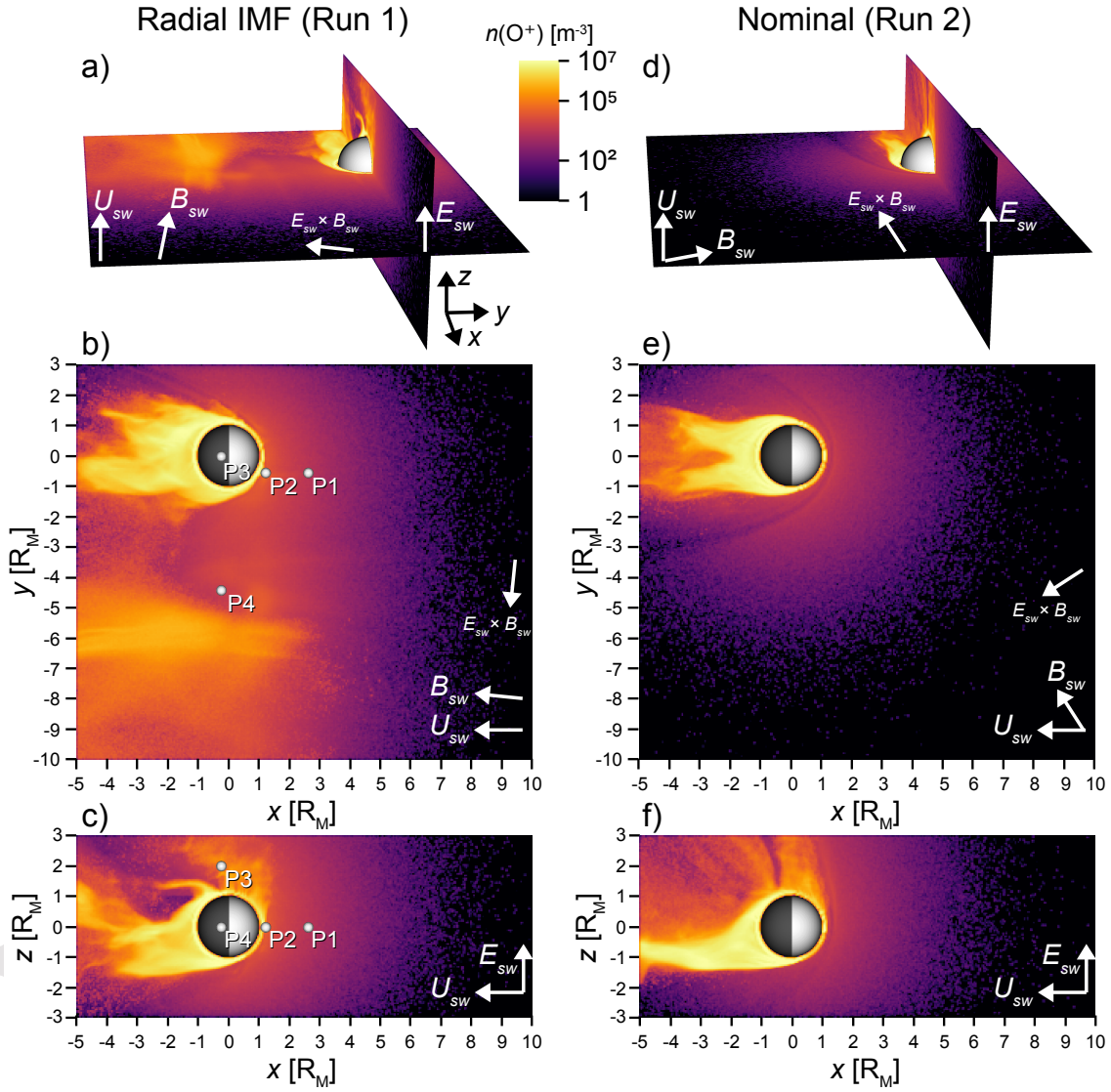
- 890 Modolo, R., S. Hess, M. Mancini, F. Leblanc, J.-Y. Chaufray, D. Brain, L. Leclercq,
 891 R. Esteban-Hernández, G. Chanteur, P. Weill, F. González-Galindo, F. For-
 892 get, M. Yagi, and C. Mazelle (2016), Mars-solar wind interaction: LatHyS,
 893 an improved parallel 3-D multispecies hybrid model, *J. Geophys. Res.*, *121*,
 894 6378–6399, 10.1002/2015JA022324.
- 895 Nilsson, H., E. Carlsson, D. A. Brain, M. Yamauchi, M. Holmström, S. Barabash,
 896 R. Lundin, and Y. Futaana (2010), Ion escape from Mars as a function of
 897 solar wind conditions: A statistical study, *Icarus*, *206*(1), 40–49, 10.1016/
 898 j.icarus.2009.03.006.
- 899 Omid, N., G. Collinson, and D. Sibeck (2020), Foreshock Bubbles at Venus: Hy-
 900 brid Simulations and VEX Observations, *J. Geophys. Res.*, *125*(2), e27056,
 901 10.1029/2019JA027056.
- 902 Parker, E. N. (1958), Dynamics of the Interplanetary Gas and Magnetic Fields.,
 903 *ApJ*, *128*, 664, 10.1086/146579.
- 904 Paschmann, G., N. Sckopke, I. Papamastorakis, J. R. Asbridge, S. J. Bame,
 905 and J. T. Gosling (1981), Characteristics of reflected and diffuse ions up-
 906 stream from the earth’s bow shock, *J. Geophys. Res.*, *86*, 4355–4364,
 907 10.1029/JA086iA06p04355.
- 908 Ramstad, R., S. Barabash, Y. Futaana, H. Nilsson, X.-D. Wang, and M. Holm-
 909 ström (2015), The Martian atmospheric ion escape rate dependence on solar
 910 wind and solar EUV conditions: 1. Seven years of Mars Express observations,
 911 *J. Geophys. Res.*, *120*(7), 1298–1309, 10.1002/2015JE004816.
- 912 Ramstad, R., S. Barabash, Y. Futaana, H. Nilsson, and M. Holmström (2017),
 913 Global Mars-solar wind coupling and ion escape, *J. Geophys. Res.*, *122*(8),
 914 8051–8062, 10.1002/2017JA024306.
- 915 Romanelli, N., C. Mazelle, J. Y. Chaufray, K. Meziane, L. Shan, S. Ruhunusiri,
 916 J. E. P. Connerney, J. R. Espley, F. Eparvier, E. Thiemann, J. S. Halekas,
 917 D. L. Mitchell, J. P. McFadden, D. Brain, and B. M. Jakosky (2016), Proton
 918 cyclotron waves occurrence rate upstream from Mars observed by MAVEN:
 919 Associated variability of the Martian upper atmosphere, *J. Geophys. Res.*,
 920 *121*(11), 11,113–11,128, 10.1002/2016JA023270.
- 921 Romanelli, N., G. DiBraccio, D. Gershman, G. Le, C. Mazelle, K. Meziane,
 922 S. Boardsen, J. Slavin, J. Raines, A. Glass, and J. Espley (2020), Upstream
 923 Ultra-Low Frequency Waves Observed by MESSENGER’s Magnetome-
 924 ter: Implications for Particle Acceleration at Mercury’s Bow Shock, *Geo-
 925 phys. Res. Lett.*, *47*(9), e87350, 10.1029/2020GL087350.
- 926 Slavin, J. A., and R. E. Holzer (1981), Solar wind flow about the terrestrial planets.
 927 I - Modeling bow shock position and shape, *J. Geophys. Res.*, *86*, 11,401–
 928 11,418, 10.1029/JA086iA13p11401.
- 929 Takahashi, K., R. L. McPherron, and T. Terasawa (1984), Dependence of the
 930 spectrum of Pc 3-4 pulsations on the interplanetary magnetic field, *J. Geo-
 931 phys. Res.*, *89*(A5), 2770–2780, 10.1029/JA089iA05p02770.
- 932 Valeille, A., M. R. Combi, V. Tennishev, S. W. Bougher, and A. F. Nagy (2010),
 933 A study of suprathermal oxygen atoms in Mars upper thermosphere and
 934 exosphere over the range of limiting conditions, *Icarus*, *206*(1), 18–27,
 935 10.1016/j.icarus.2008.08.018.
- 936 Yamauchi, M., T. Hara, R. Lundin, E. Dubinin, A. Fedorov, J. A. Sauvaud, R. A.
 937 Frahm, R. Ramstad, Y. Futaana, M. Holmstrom, and S. Barabash (2015),
 938 Seasonal variation of Martian pick-up ions: Evidence of breathing exosphere,
 939 *Planet. Space Sci.*, *119*, 54–61, 10.1016/j.pss.2015.09.013.
- 940 Zhang, T. L., J. Du, Y. J. Ma, H. Lammer, W. Baumjohann, C. Wang, and
 941 C. T. Russell (2009), Disappearing induced magnetosphere at Venus: Im-
 942 plications for close-in exoplanets, *Geophys. Res. Lett.*, *36*, 20,203, 10.1029/
 943 2009GL040515.



598 **Figure 1.** Overview of the Mars simulation run (a-c: Run 1, d-f: Run 2) snapshots at $t =$
 599 750 s. The coloring gives the solar wind proton temperature at the xy ($z = 0$) and xz ($y = 0$)
 600 planes and the gray lines display the magnetic field lines. Three-dimensional field line tracing
 601 was started in the upstream region on the $z = 400$ km plane. The sphere shows the radius of
 602 Mars for context. The black and white arrows give the orientation of the coordinate axes and the
 603 undisturbed upstream solar wind bulk velocity (\vec{U}_{sw}), IMF (\vec{B}_{sw}) and convection electric field
 604 (\vec{E}_{sw}) vectors. See also Movie S01 in the supplementary material.

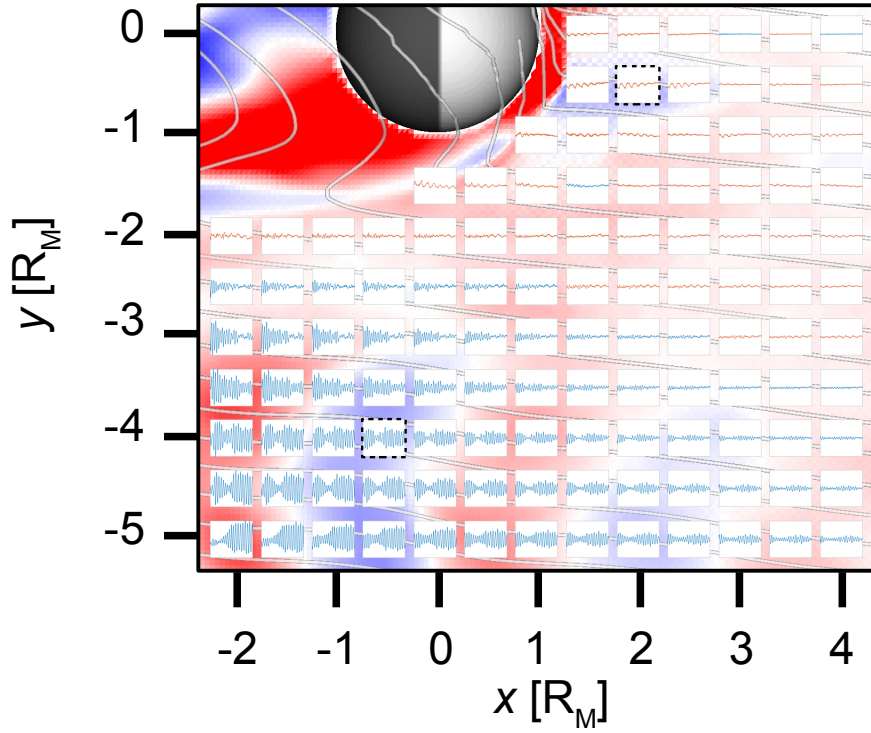


605 **Figure 2.** B_z component of the magnetic field (a: Run 1, b: Run 2) at the xy ($z = 0$) plane
 606 at $t = 750$ s. The gray lines display the magnetic field lines projected on the $z = 0$ plane. The
 607 figure format and the field lines are the same as in Fig. 1b,e. See also Movie S01 in the supple-
 608 mentary material.

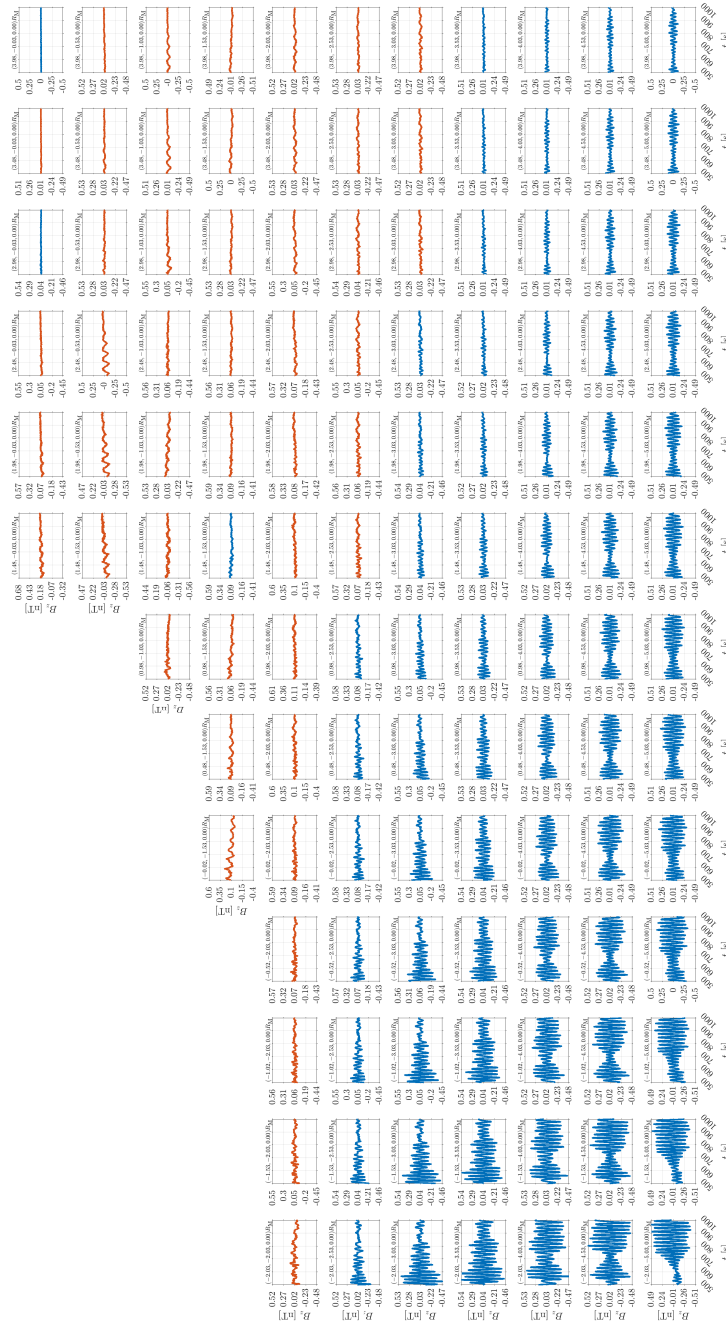


609
610
611
612
613

Figure 3. Overview of the O^+ density in Run 1 and Run 2 at $t = 750$ s. The figure is in the same format as Fig. 1. The $\vec{E}_{SW} \times \vec{B}_{SW}$ arrows give the orientation of the undisturbed upstream $E \times B$ drift velocity. P1-P4 in panels b and c display the locations of points where virtual spacecraft time series and ion velocity distributions were determined. See also Movie S02 in the supplementary material.

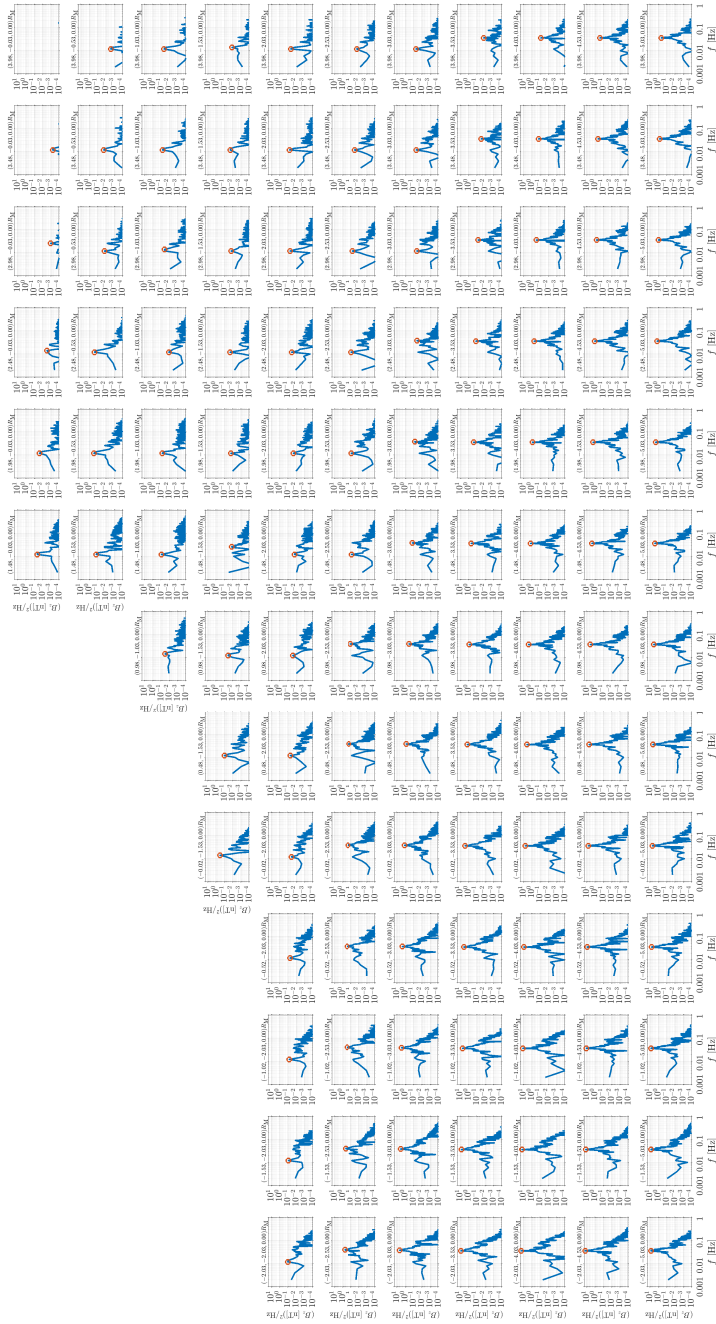


614 **Figure 4.** Spatial map of time series of the B_z component of the magnetic field in the foreshock in the radial IMF run at the xy ($z = 0$) plane. The background B_z figure with the mag-
 615 netic field lines is the same as in Fig. 2a. The inserts show $B_z(t)$ with time on the horizontal
 616 axis and B_z on the vertical axis. The vertical axis is centered at the mean value
 617 of B_z in each point and the axis limits are $\text{mean}(B_z) \pm 0.5$ nT. Both axes are linear. Each insert
 618 is centered around the point from where the time series was interpolated. Periods above 40 s
 619 are drawn in red and periods below 40 s in blue. The dashes lines show the locations where the
 620 minimum variance analysis is performed in Figs. 8 and 9. See Fig. 5 for a detailed version of the
 621 inserts.
 622

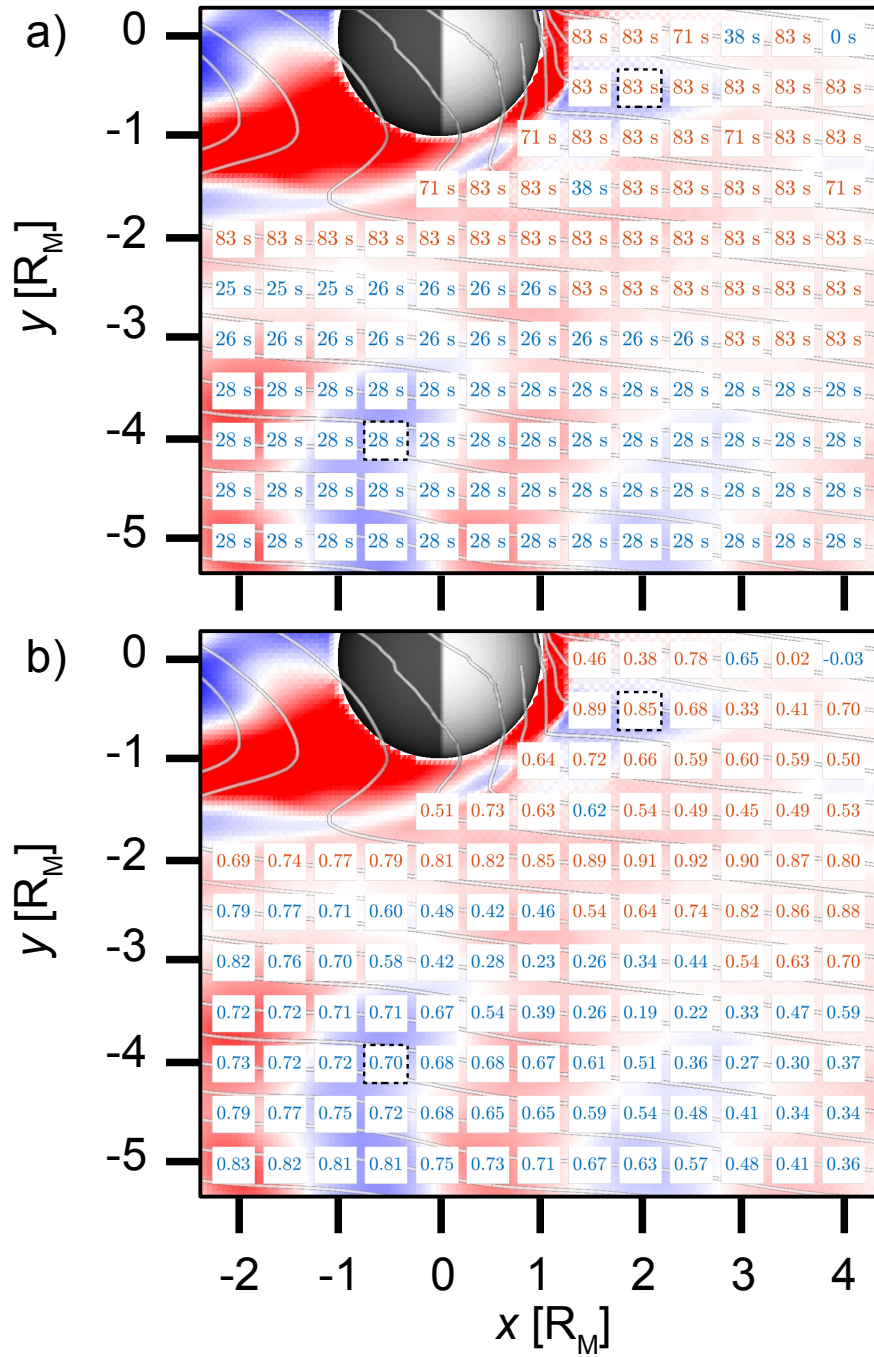


623 **Figure 5.** Detailed time series of B_z in Fig. 4. Panel titles give the coordinates of the points. The
 624 panels are organized in the rotated figure to increase the readability as follows: the x -coordinate increases
 625 from the bottom of the page to the top and the y -coordinate increases from right to left.

Accepted Article

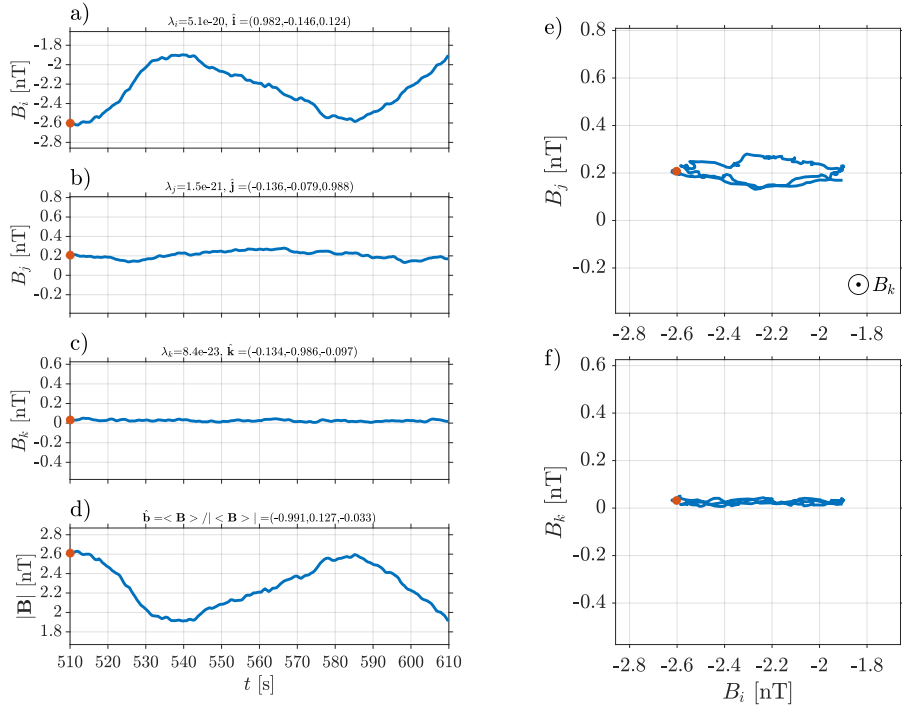


626 **Figure 6.** Power spectral density (PSD) of $B_z(t)$ in Fig. 5. Red circles denote the maximum PSD, where
 627 periods above 100 s or power spectral densities less than 2×10^{-4} nT²/Hz were ignored. A detrending with a
 628 running average over 100 s was applied before taking the fast Fourier transformation. The panels are organized
 629 in the same way as in Fig. 5.

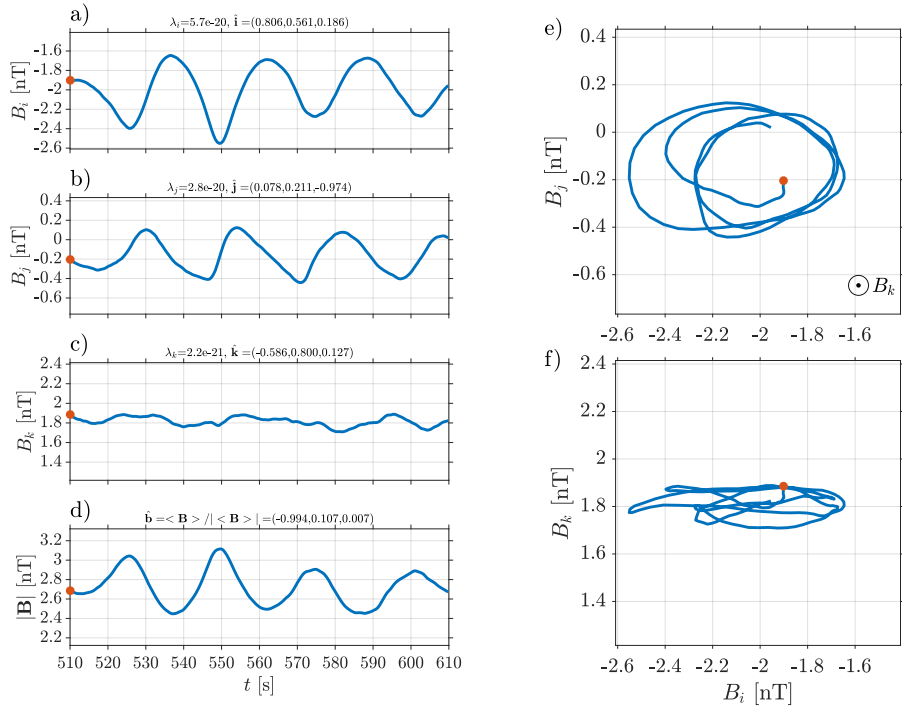


630
631
632
633

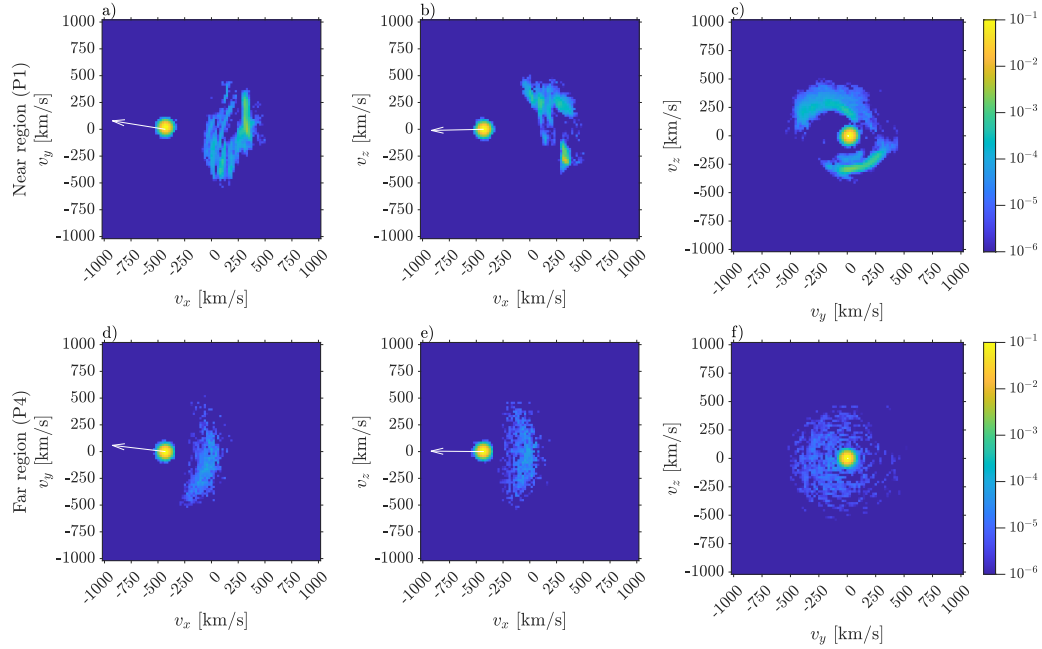
Figure 7. Spatial map of the foreshock ULF wave properties: (a) the maximum power spectral density periods of B_z determined in Fig. 6, and (b) the Pearson correlation coefficient between the electron density and the magnitude of the magnetic field. Periods above 40 s are written in red and periods below 40 s in blue. The figure is in the same format as Fig. 4.



634 **Figure 8.** Minimum variance analysis (MVA) of the magnetic field in the near foreshock
 635 region. The point location is marked as dashed line around the insert in upper right quadrant
 636 in Fig. 4. (a-c) Left panels show the components of the magnetic field in the MVA coordinate
 637 system. In the left panel titles, λ_i , λ_j and λ_k give the eigenvalues of the magnetic variance ma-
 638 trix and \hat{i} , \hat{j} and \hat{k} are the unit vectors of the maximum, intermediate and minimum variance
 639 directions in the simulation coordinate system, respectively. The title of panel (d) gives the unit
 640 vector of the average magnetic field (\hat{b}) in the simulation coordinate system in the MVA analysis
 641 period. (e) The hodogram of the magnetic field on the plane of the maximum and intermediate
 642 variance directions. (f) The hodogram of the magnetic field on the plane of the maximum and
 643 minimum variance directions. The red dots denote the start of the time series.



644 **Figure 9.** Minimum variance analysis (MVA) of the magnetic field in the far foreshock region.
 645 The point location is marked as dashed line around the insert in lower left quadrant in Fig. 4.
 646 The figure is in the same format as Fig. 8.



647 **Figure 10.** Solar wind proton (H_{SW}^+) velocity distributions in the near foreshock region at
 648 P1 (a-c) and in the far foreshock region at P4 (d-f) integrated over $t = 500 \dots 800$ s. The plots
 649 are projections of the whole three-dimensional distribution collapsed on the (v_x, v_y) , (v_x, v_z) and
 650 (v_y, v_z) planes. The white arrows give the orientation of the average magnetic field vector pro-
 651 jected on the planes over the same time interval. The coloring is the number of particles in each
 652 velocity bin divided by the total number of particles in the panel.

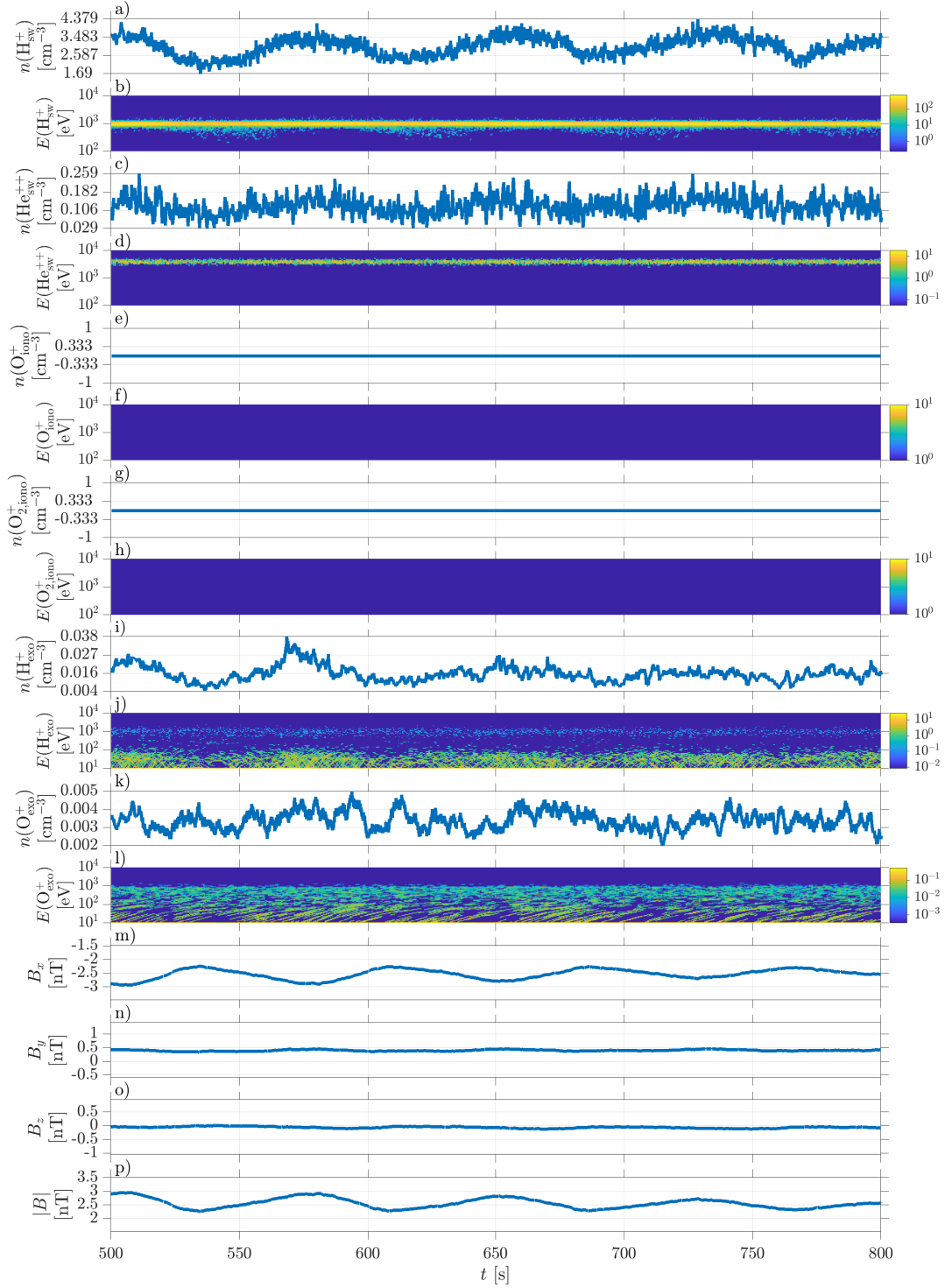


Figure 11. Virtual spacecraft time series of ions and magnetic field at P1 (dayside foreshock). Panels a-l show the density (n) and omni-directional time-energy spectrogram (E) of different ion populations and panels m-p show the magnetic field (B). The ion populations are the solar wind protons (H_{sw}^+), the solar wind alphas (He_{sw}^{++}), the ionospheric atomic oxygen (O_{30}^{+}), the ionospheric molecular oxygen ($O_{2,iono}^+$), the exospheric hydrogen photoions (H_{exo}^+) and the exospheric oxygen photoions (O_{exo}^+). The coloring of the the omni-directional spectra were determined as $\sum_i w_i v_i / (4\pi \Delta V \Delta E)$ [$s^{-1} m^{-2} eV^{-1} sr^{-1}$], where

653

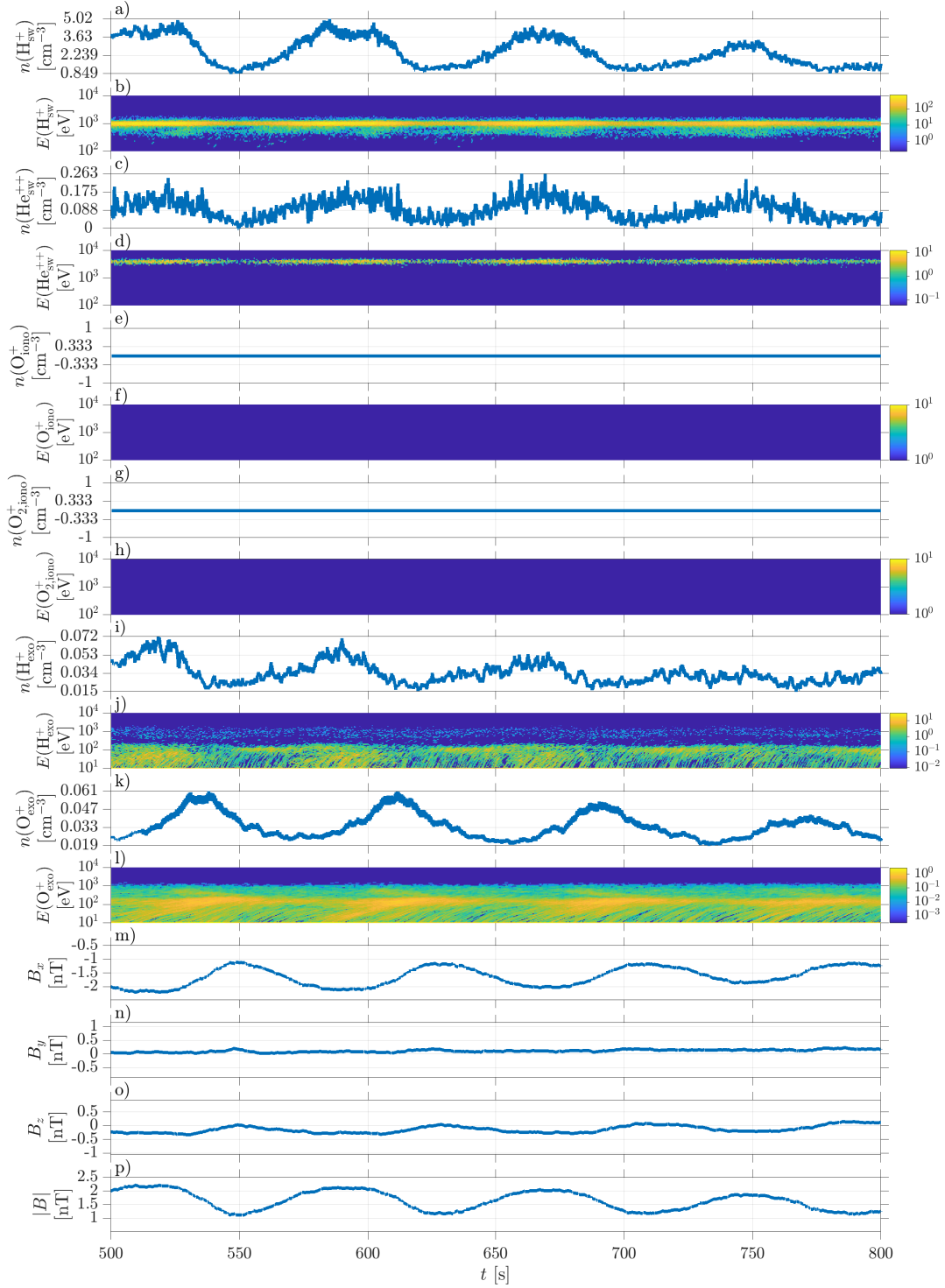
654

655

656

657

658

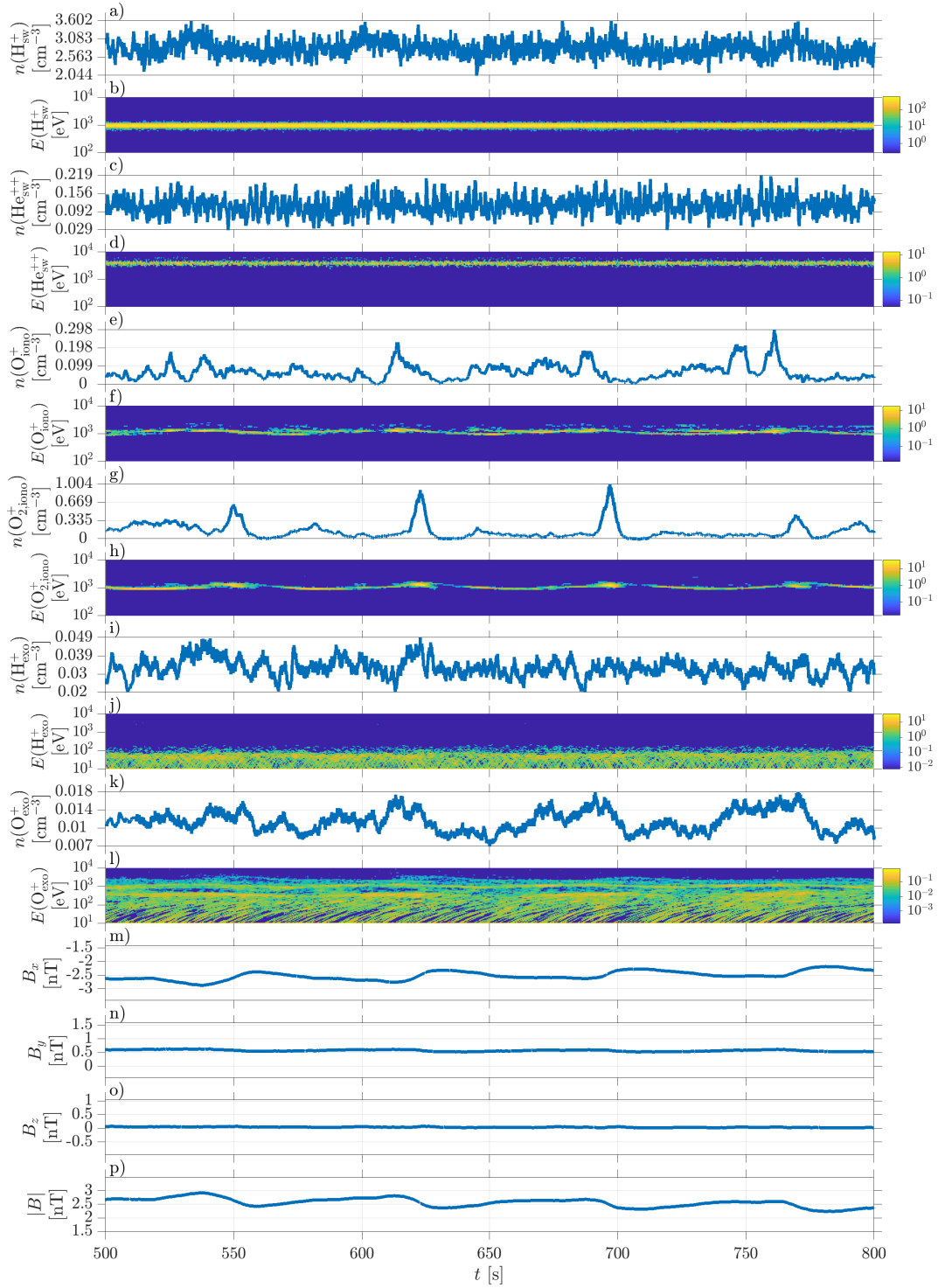


663

Figure 12. Virtual spacecraft time series of ions and magnetic field at P2 (subsolar magnetosheath). The figure is in the same format as Fig. 11.

664

This article is protected by copyright. All rights reserved.



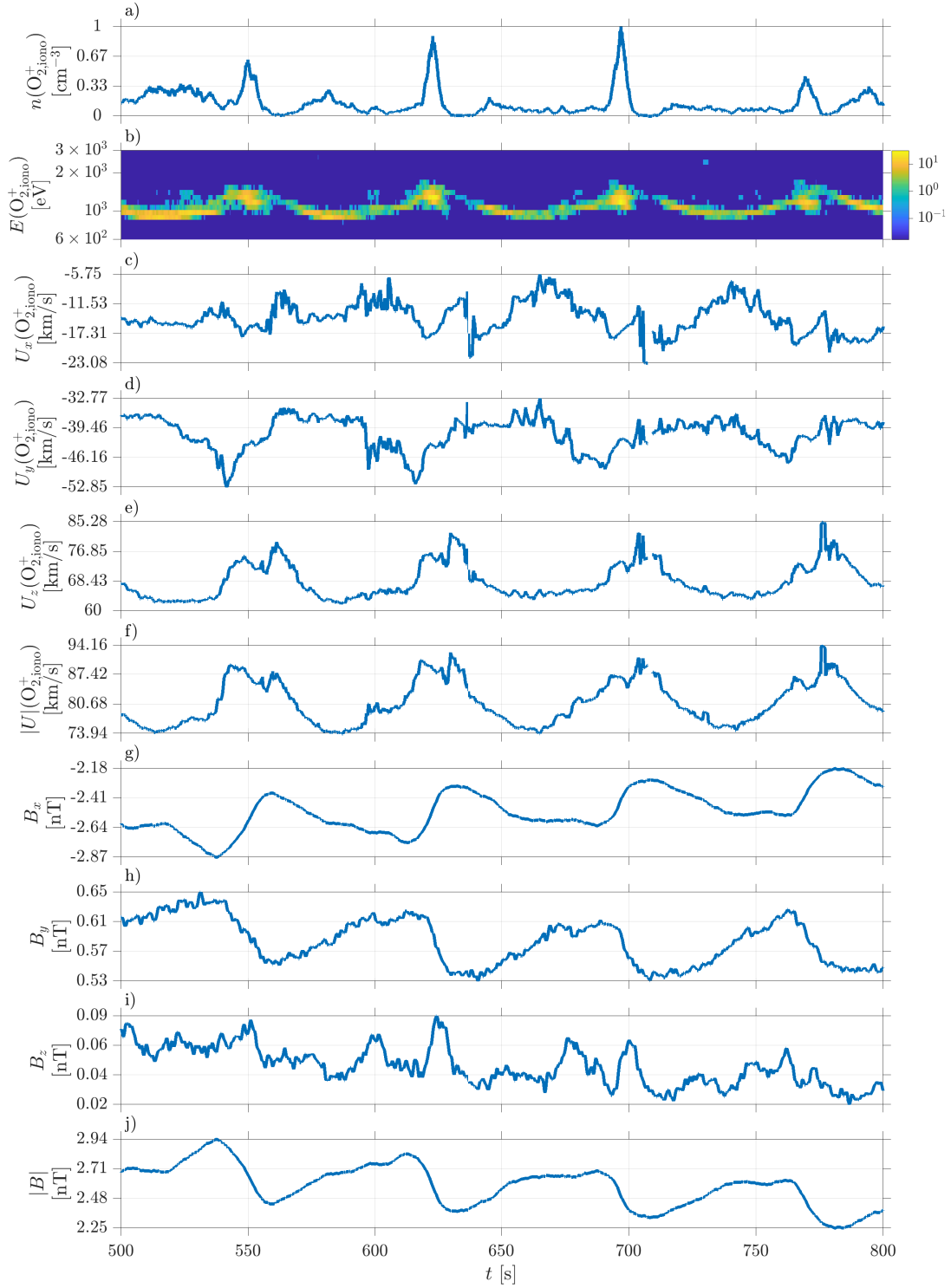
665

Figure 13. Virtual spacecraft time series of ions and magnetic field at P3 (heavy ion plume).

666

The figure is in the same format as Fig. 11.

This article is protected by copyright. All rights reserved.



667

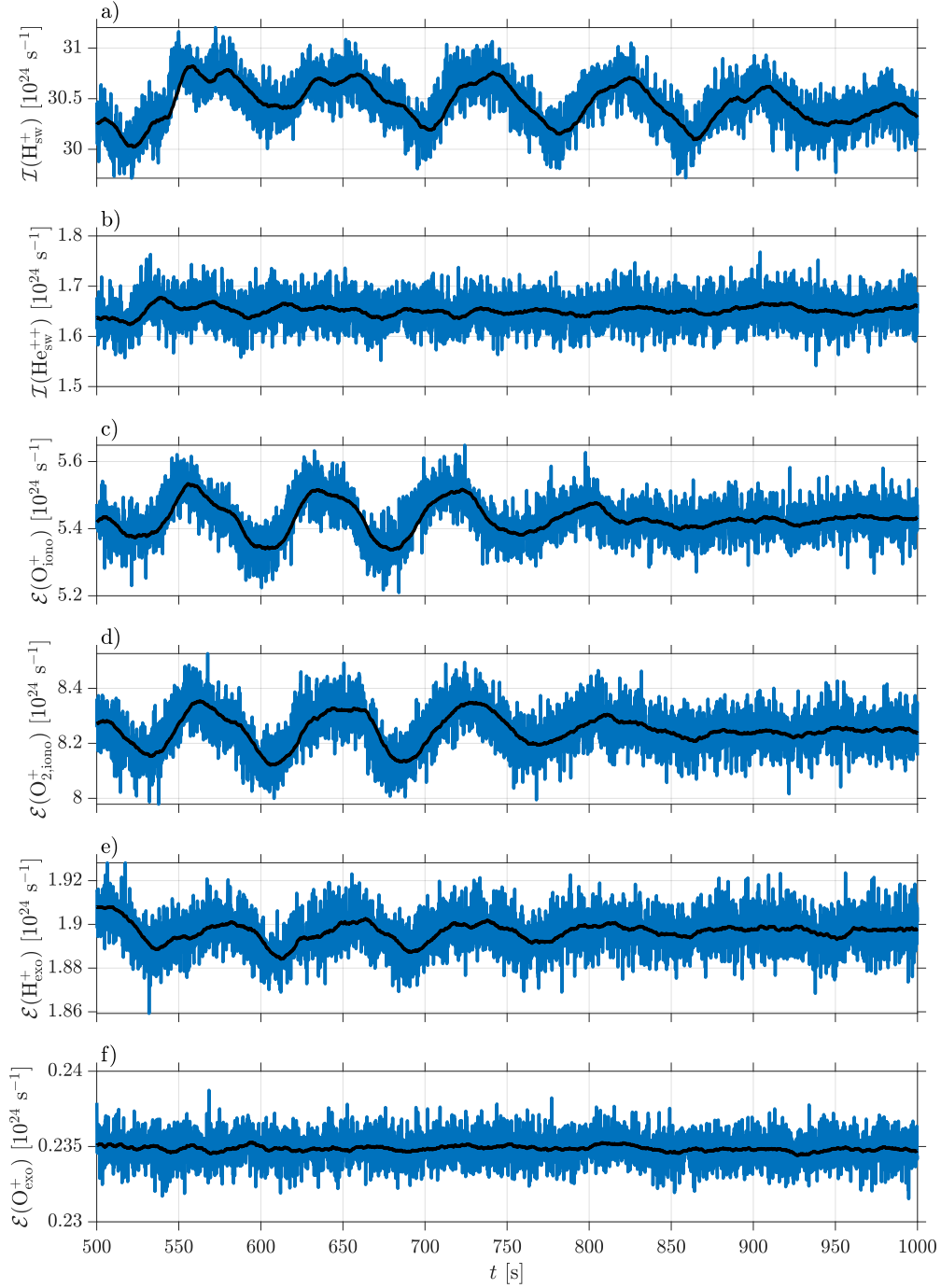
Figure 14. Virtual spacecraft time series of ionospheric O_2^+ ions at P3 (heavy ion plume).

668

The topmost panels give the density (n) and the time-energy spectrogram (E) followed by the

669

This article is protected by copyright. All rights reserved.



670 **Figure 15.** Time series global solar wind ion precipitation rates (\mathcal{I}) (a and b) and global
 671 planetary ion escape rates (\mathcal{E}) (c-f) in the radial IMF run. The black line gives the running average over 10 s.
 672